



HAL
open science

Study of the performance of SiO₂ supported Mo₂C and metalpromoted Mo₂C catalysts for the hydrodeoxygenation of m-cresol

Leticia Sosa, Priscilla de Souza, Raphaela Rafael, Robert Wojcieszak, Valérie Briois, Lucas Francisco, Raimundo Rabelo-Neto, Eric Marceau, Sébastien Paul, Fabio Toniolo, et al.

► To cite this version:

Leticia Sosa, Priscilla de Souza, Raphaela Rafael, Robert Wojcieszak, Valérie Briois, et al.. Study of the performance of SiO₂ supported Mo₂C and metalpromoted Mo₂C catalysts for the hydrodeoxygenation of m-cresol. *Applied Catalysis B: Environmental*, 2023, 331, pp.122720. 10.1016/j.apcatb.2023.122720 . hal-04786712

HAL Id: hal-04786712

<https://hal.science/hal-04786712v1>

Submitted on 16 Nov 2024

HAL is a multi-disciplinary open access archive for the deposit and dissemination of scientific research documents, whether they are published or not. The documents may come from teaching and research institutions in France or abroad, or from public or private research centers.

L'archive ouverte pluridisciplinaire **HAL**, est destinée au dépôt et à la diffusion de documents scientifiques de niveau recherche, publiés ou non, émanant des établissements d'enseignement et de recherche français ou étrangers, des laboratoires publics ou privés.



Distributed under a Creative Commons Attribution - NonCommercial - NoDerivatives 4.0 International License

Study of the performance of SiO₂ supported Mo₂C and metal-promoted Mo₂C catalysts for the hydrodeoxygenation of m-cresol

Leticia F. Sosa^{1,2}, Priscilla M. de Souza², Raphaela A. Rafael², Robert Wojcieszak²,
Valérie Briois³, Lucas R. Francisco^{4,5}, Raimundo C. Rabelo-Neto⁴, Eric Marceau²,
Sébastien Paul², Fabio S. Toniolo¹, Fabio B. Noronha^{2,4,5*}

¹ Federal University of Rio Janeiro, Chemical Engineering Program of COPPE/UFRJ, P.O. Box 68502, CEP 21941-972, Rio de Janeiro, Brazil.

² Univ. Lille, CNRS, Centrale Lille, Univ. Artois, UMR 8181 - UCCS - Unité de Catalyse et Chimie du Solide, F-59000 Lille, France.

³ Synchrotron SOLEIL, L'Orme des Merisiers, Saint-Aubin, BP 48, 91192 Gif-sur-Yvette Cedex, France.

⁴ National Institute of Technology, Catalysis, Biocatalysis and Chemical Processes Division, Av. Venezuela 82, 20081-312, Rio de Janeiro, RJ, Brazil.

⁵ Military Institute of Engineering, Chemical Engineering Department, Praça Gal. Tiburcio 80, Rio de Janeiro, 22290-270, Brazil.

Corresponding author: fabio.bellot@int.gov.br

Submitted to Applied Catalysis B: Environmental

September 2022

Abstract

The catalytic performance of different Mo carbides, including an unsupported Mo₂C and SiO₂-supported carbides promoted or not with Ni/Cu, was investigated in the hydrodeoxygenation (HDO) of m-cresol at 300 °C and ambient pressure. To get more insight into the effect of the promoters during the synthesis of the Mo carbides, the carburization of the supported catalysts was followed by X-ray spectroscopy (XAS) under 20 % (v/v) CH₄/H₂. The results showed that the presence of a second metal promotes the first step of reduction and it is related to the crystallinity of the initial promoter species, but that it does not assist the carburizing step. All carbides proved to be highly selective in performing the direct deoxygenation of m-cresol, since high yields to toluene were achieved (> 96 %). The addition of Ni to the Mo carbide promoted the activity of the catalysts, but also generated ring hydrogenation products.

Keywords: Hydrodeoxygenation; m-cresol; molybdenum carbide; Ni-promoted molybdenum carbide; Cu-promoted molybdenum carbide.

1. Introduction

In the last decades, lignocellulosic biomass has been pointed out as a potential sustainable raw material for the production of energy, biofuels, and chemicals of industrial interest [1,2]. The fast pyrolysis of lignocellulosic biomass generates bio-oil, which can be used for the production of hydrocarbons that are compatible with petroleum-derived fuels. However, large amounts of oxygen-rich phenolic compounds such as cresol, guaiacol, and phenol can be found in bio-oils. The high content of oxygen makes the bio-oil to have undesirable properties like low calorific value, high acidity, and viscosity, thermal and chemical instability. The catalytic hydrodeoxygenation (HDO) is a key step to upgrade bio-oil to liquid fuels by removing oxygen [3–5].

Since lignin-derived bio-oil mainly contains functionalized aromatic compounds, the design of new catalysts for the HDO reaction is based on model molecules that have hydroxyl and methoxy functional groups such as phenol [6–8], cresol [9–11], anisole [12–14] and guaiacol [15–17]. According to these studies, a bifunctional catalyst containing a metal particle to carry out hydrogenation/hydrogenolysis reactions and a support responsible for deoxygenation is required for the HDO of phenolic compounds [18].

For the HDO of phenol and m-cresol, it has been proposed that the reaction follows the tautomerization mechanism that contains three main reaction pathways: (i) the sequential hydrogenation of the aromatic ring from the keto tautomer intermediate formed, producing cyclohexanone/methylcyclohexanone and cyclohexanol/methylcyclohexanol; (ii) the hydrogenation of the carbonyl group from the tautomer with the formation of an unsaturated alcohol that is dehydrated to

benzene/toluene; (iii) the direct deoxygenation of the tautomer, producing benzene/toluene [19–21].

In the tautomerization mechanism, the type of the metal and support affects significantly the HDO reaction pathways [11,22–26]. The hydrogenation of the ring is promoted by metals such as Pt, Pd, Ni, and Co as well as supports like SiO₂, Al₂O₃, and CeO₂. On the other hand, the deoxygenation route is favored on oxophilic metals and supports such as Ru, Fe, ZrO₂, TiO₂, and Nb₂O₅. Despite their high deoxygenation capacity, the oxophilic metal such as Ru promotes the hydrogenolysis reaction of the intermediate formed, producing large amounts of methane and C₂-C₅ hydrocarbons. In the case of Fe, its incomplete reduction may produce Lewis acid sites that catalyze the alkylation reactions. Therefore, all these metals present some drawbacks in producing deoxygenated products with high selectivity.

Transition metal carbides (TMC) exhibit similar catalytic performances to noble metals, but they are cheaper [27]. Recently, they have been pointed out as being quite selective for breaking C=O, C-OH, and C-O-C bonds [28–30]. For this reason, they have been evaluated for HDO reactions of several phenolic compounds such as phenol [31,32], m-cresol [33,34], anisole [35–37], and guaiacol [38–43].

Recently, the catalytic performance of a molybdenum carbide supported on activated carbon (AC) was compared to that of noble metal-based catalysts (Ru and Pd) for the HDO of guaiacol. Despite having a lower reaction rate for guaiacol conversion among the catalysts, the Mo₂C/AC was the most selective to yield deoxygenated products such as phenol with minimal consumption of H₂, whereas ring hydrogenation products were also produced over Ru and Pd catalysts [43].

Temperature programmed carburization (TPC) is the most widely used technique to synthesize TMC. In this methodology, a metal oxide is heated at a specific rate in a

carburizing atmosphere containing CO or a hydrocarbon (CH_4 , C_2H_6 , C_3H_8 , C_4H_{10}) used as a carbon source, co-fed or not with hydrogen [44]. In general, when a mixture of CH_4/H_2 is used in the TPC, the synthesis is monitored by mass spectroscopy and the signals of water ($m/z = 18$) and CO ($m/z = 28$) related to the reduction of the metal oxide and formation of the carbide, respectively, are accompanied [45]. The profiles obtained give an idea of the temperature ranges in which the transformations take place, but it is difficult to make inferences about the chemical changes of the species, especially in more complex systems such as for bimetallic carbides.

The use of bimetallic carbides are advantageous, because they exhibit higher catalytic activity than monometallic carbides [46–50]. In addition, the presence of a second metal (Pt, Pd, Ni, Co, Cu) to MoO_3 is reported to lower the first stage of reduction (MoO_3 to MoO_2 or an oxycarbide) by 100 - 250 °C during the carburization under a CH_4/H_2 atmosphere, which is caused by the ability of the metals in activate hydrogen [50].

In this sense, X-ray absorption spectroscopy (XAS) is a powerful technique that allows the monitoring of the species formed during the *in situ* carburization. To the best of your knowledge, XAS analysis has been used to investigate Ni-Mo/Cu-Mo bimetallic carbides only after their synthesis [51,52] and not during carburization.

Taking this into account, the main goals of this work are: (i) investigating the *in situ* carburization of a monometallic and bimetallic SiO_2 -supported Mo carbides promoted with Ni and Cu by XAS; (ii) evaluating the catalytic performance of Mo carbides for the HDO of m-cresol in the gas phase; and (iii) compare their performance to that of noble metal-based catalysts in the literature.

2- Experimental

2.1 Catalyst preparation

In this work, silica (SiO_2 , Aerosil 200, Evonik Industries) was used as support. The material was moistened with deionized water, dried under static air for 3 h at 120 °C, and heated at 500 °C (10 °C min^{-1}) for 6 h. The precursors of the monometallic and Ni/Cu promoted molybdenum carbides supported on silica ($\text{Mo}_2\text{C/SiO}_2$, Ni- $\text{Mo}_x\text{C}_y/\text{SiO}_2$, and Cu- $\text{Mo}_x\text{C}_y/\text{SiO}_2$) were prepared by incipient wetness impregnation of the support to achieve 20 wt. % of active phase (20 % for the monometallic and 17 % Mo and 3 % Ni or Cu for the promoted materials).

To prepare the monometallic carbide, an adequate amount of ammonium heptamolybdate ($(\text{NH}_4)_6\text{Mo}_7\text{O}_{24}\cdot 4\text{H}_2\text{O}$, Sigma-Aldrich) was first solubilized in distilled water and then the solution obtained (0.173 g mL^{-1}) was impregnated on the support. During the impregnation, the material was dried several times at 110 °C for 1 h until the solution was depleted. A final drying was performed overnight at the same temperature.

For the promoted catalysts, adequate amounts of nickel nitrate ($\text{Ni}(\text{NO}_3)_2\cdot 6\text{H}_2\text{O}$, Sigma-Aldrich) or copper nitrate ($\text{Cu}(\text{NO}_3)_2\cdot \text{H}_2\text{O}$, Sigma-Aldrich) and ammonium heptamolybdate ($(\text{NH}_4)_6\text{Mo}_7\text{O}_{24}\cdot 4\text{H}_2\text{O}$, Sigma-Aldrich) were solubilized individually in distilled water at the concentrations of 0.076, 0.045 and 0.16 g mL^{-1} , respectively. Firstly, the solution containing Mo was impregnated on the support and dried at 110 °C for 1 h until it was depleted. After that, the material was dried overnight at the same temperature and then the solution containing Ni or Cu was added using the same procedure.

For the sake of comparison, two reference catalysts containing 3 wt. % of Ni/Cu supported on SiO₂ were prepared by incipient wetness impregnation. For this, adequate amounts of nickel nitrate (Ni(NO₃)₂·6H₂O, Sigma-Aldrich) or copper nitrate (Cu(NO₃)₂·H₂O, Sigma-Aldrich) were solubilized in distilled water at the concentrations of 0.117 and 0.087 g mL⁻¹, respectively, and then each solution was impregnated individually on the support. After impregnation, the materials were dried at 110 °C overnight. Finally, all samples were treated under static air at 500 °C (5 °C min⁻¹) for 3 h to obtain the calcined precursors.

To synthesize an unsupported and the SiO₂-supported Mo carbides, 1 g of molybdenum trioxide (MoO₃, Sigma-Aldrich) or calcined precursor, respectively, were carburized at 650 °C (2.5 °C min⁻¹) for 2 h with 20 % (v/v) CH₄/H₂ (200 mL min⁻¹ STP) [53]. The Me carbides were designated as Mo₂C, Mo₂C/SiO₂, Ni-Mo_xC_y/SiO₂, and Cu-Mo_xC_y/SiO₂ and the reference catalysts as Ni/SiO₂ and Cu/SiO₂. When necessary, the catalysts were passivated at room temperature for 14 h with 0.5 % (v/v) O₂/N₂ (30 mL min⁻¹ STP) due to their pyrophoric nature.

2.2. Catalyst characterization

The amount of Mo, Ni, and Cu in the carbides was determined by inductively coupled plasma optical emission spectrometry (ICP-OES) using a 720-ES ICP-OES spectrometer (Agilent) with axial viewing and simultaneous CCD detection. The content of carbon was determined by elemental analysis using a Thermo Scientific FlashSmart automated analyzer.

Textural properties of SiO₂ and passivated catalysts were measured by nitrogen adsorption at -196 °C using a Micromeritics TriStar II Plus analyzer. The samples were previously outgassed under vacuum firstly at 75 °C for 1 h and then at 300 °C for up to

24 h. Specific surface areas and the total pore volume were estimated using the Brunauer-Emmett-Teller (BET) and the Barrett-Joyner-Halenda (BJH) methods, respectively.

X-ray absorption spectroscopy (XAS) was carried out in the transmission mode at the ROCK Quick-EXAFS beamline at the French SOLEIL synchrotron radiation facility [54]. The beamline benefits from a 2.81 Tesla Super-Bend source which delivers nearly 10^{12} ph s^{-1} between 8 to 20 keV. Spectra were acquired under *in situ* conditions, either at the Mo K-edge for monometallic systems, or at the Ni (8333 eV) / Cu (8979 eV) and Mo (20000 eV) K-edges for the bimetallic Ni-Mo and Cu-Mo systems during carburization under 20 % (v/v) CH₄/H₂. The monochromator used is based on a Si (111) channel-cut installed on a tilt table allowed to oscillate around the Bragg angle characteristic of the element of interest, i.e., 13.4332° for Ni, 12.2886° for Cu, and 5.6550° for Mo, with an amplitude of 2.0° for Ni and Cu and 0.5° for Mo. The Si (111) channel-cut oscillation frequency was set to 2 Hz and recorded two quick-EXAFS spectra every 0.5 s. Every 10 acquired spectra were merged to improve the signal/noise ratio. Ionization chambers were filled with nitrogen for Ni and Cu K edges measurements and a mixture of 50:50 of nitrogen and argon for the Mo K edge measurements. The beam size at the sample position was ~ 500 μm (H) x 300 μm (V).

Experiments were performed using a dedicated gas-feeding set-up installed on the ROCK beamline [55]. A quartz capillary (1.5 mm x 80 mm x 0.04 mm) was used as sample holder. The powder catalyst bed (length ~ 8 - 9 mm) was maintained at the center of the capillary between two pieces of quartz wool and heated using a gas blower. The *in situ* temperature programmed carburization of the calcined precursors was performed by heating the cell from room temperature to 650 °C (2.5 °C min⁻¹) under a 20 % (v/v) CH₄/H₂ flow (5 mL min⁻¹ STP). A reactivation at 400 °C (5 °C min⁻¹) under a H₂ flow (5 mL min⁻¹ STP) was performed for the Mo₂C catalysts that had been previously passivated. All experiments were

kept isothermal until no changes were observed in the spectra. Spectra were then recorded back at room temperature.

Energy calibration concerning the reference metal foil (Mo, Ni, Cu) and a XAS data-normalization procedure was first carried out using the Python normal graphical interface developed at SOLEIL for the fast handling of Quick-XAS data [56]. The EXAFS signal extraction and Fourier transform of the EXAFS spectra were done using the Athena graphical interface software [57]. EXAFS fitting of coordination numbers (N), Debye–Waller factors (σ^2), and interatomic distances (R) was simultaneously performed on k-, k^2 - and k^3 -weighted $\chi(k)$ functions with the Artemis interface to IFFFIT using least-squares refinements [58]. Fits were first performed on the metallic foil references for the determination of the S_0^2 factor. Fourier-transformed EXAFS signals are presented as $k^3\chi(k)$ functions and Fourier transforms are shown without phase correction.

The proportions of the different Mo, Ni, and Cu species during the different stages of carburization were determined by a chemometric procedure, the Multivariate Curve Resolution by Alternative-Least Squares (MCR-ALS) methodology, using the free MCR-ALS GUI 2.0 toolbox developed by the Tauler group on the Matlab platform [59]. XAS spectra are considered to be linear combinations of individual spectral components (matrix S) weighted by their concentration that varies with temperature or time (matrix C). The determination of matrices S and C takes place without initial hypotheses on the chemical nature of the different species appearing along the thermal treatment, by a least-square minimization of a residue matrix. The determination of the most likely number of spectral components takes place via a preliminary Principal Component Analysis by Singular-Value Decomposition (PCA-SVD). MCR-ALS spectral components (XANES spectra, EXAFS oscillations, and Fourier transform) are

then identified to successive species after checking their chemical meaningfulness, by comparison with spectra of compounds already known in the mixture or as standards, or with plausible models in accordance with the chemistry of the system. Further details about the MCR-ALS method applied to XAS are available in recent publications [56,60,61].

RAMAN

The synthesis of carbides was also accompanied by temperature-programmed carburization (TPC) in a multipurpose unit coupled to a Pfeiffer Vacuum mass spectrometer (MS) model QME 200. Before analysis, the calcined precursors (0.1 g) were treated under He (50 mL min⁻¹ STP) at 200 °C (10 °C min⁻¹) for 1 h to eliminate water, and then cooled down to 30 °C. Then, He was replaced by 20 % (v/v) CH₄/H₂ (100 mL min⁻¹ STP) and then, the temperature was increased up to 800 °C (2.5 °C min⁻¹). The signals of the ions $m/z = 18$ (H₂O), $m/z = 15$ (CH₄) and $m/z = 28$ (CO) were continuously monitored on the mass spectrometer.

The metallic dispersion of the catalysts was estimated by CO chemisorption in a multipurpose unit coupled to a Pfeiffer Vacuum mass spectrometer (MS) model QME 200 using the pulse method. Before the analysis, the calcined precursors (200 mg) were carburized *in situ* at 650 °C (2.5 °C min⁻¹) for 2 h under 20 % (v/v) CH₄/H₂ (100 mL min⁻¹ STP) and then cooled to room temperature (RT) in a He atmosphere (50 mL min⁻¹ STP). Once RT was reached, He was switched to a mixture of 5 % (v/v) CO/He (50 mL min⁻¹ STP) and waited until the signal corresponding to CO ($m/z = 28$) had stabilized in the mass spectrometer with the reactor in by-pass. After stabilizing, the reactor valve was opened and CO chemisorption was performed for 15 min. Three pulses of He (50 mL min⁻¹ STP) of known volume (2.39 mL) were injected for quantification. After that, the catalyst surface was purged with He (50 mL min⁻¹ STP) for 30 min, and the same

procedure was repeated. The area obtained in the first step corresponds to the chemisorption, physisorption and dead volume of the reactor, while the area of the second step is ascribed to the physisorption, and dead volume of the reactor, the difference between them gives the area corresponding to the chemisorbed CO. For the quantification, it was assumed a stoichiometry of one CO molecule per Mo₂C, Ni, and Cu surface.

2.3. Catalytic evaluation

The HDO of m-cresol reaction was performed in a vapor-phase fixed-bed flow reactor system, operating at atmospheric pressure of H₂ and 300 °C. The samples were mixed with silicon carbide ($m_{\text{SiC}}/m_{\text{catalyst}} = 3.0$) to make the flow more uniform and to avoid hot spot formation or flow channeling. The catalysts were first synthesized *in situ* at 650 °C (2.5 °C min⁻¹) for 2 h using 20 % (v/v) CH₄/H₂ (100 mL min⁻¹ STP) mixture. Then, the temperature was decreased to 300 °C and the reactant mixture was obtained by flowing 60 mL min⁻¹ STP of H₂ through a saturator containing the probe molecule that was maintained at the temperature needed to produce the desired H₂/organic molecule mole ratio of 60 (87 °C).

Different W/F ratios (catalyst mass/mass flow rate of the oxygenated compound) were used for each catalyst to achieve low conversions. The first injection was carried out after 5 min of time-on-stream (TOS), where minimal deactivation of the catalyst was expected. The reaction products were analyzed using an Agilent Technologies GCMS (7890A/5975C), equipped with an HP-Innowax capillary column and a flame-ionization detector (FID).

The conversion, product selectivity, and HDO reaction rate were determined by the following equations (1-3):

$$\text{Conversion (\%)} = \frac{\text{mol}_{\text{feed}}^0 - \text{mol}_{\text{feed}}}{\text{mol}_{\text{feed}}^0} \times 100 \quad (1)$$

$$\text{Selectivity (\%)} = \frac{\text{mol}_i}{\text{mol}_{\text{feed}}^0 - \text{mol}_{\text{feed}}} \times 100 \quad (2)$$

$$\text{Rate}_{\text{HDO}} (\text{mmol } g_{\text{cat}}^{-1} \text{ min}^{-1}) = \frac{\text{yield of deoxygenated product} \times F}{W} \quad (3)$$

where $\text{mol}_{\text{feed}}^0$ and mol_{feed} are the numbers of initial and after reaction moles of the organic feed respectively, mol_i is the number of moles of a given i product and W is the catalyst mass (g).

3. Results and discussion

3.1 Characterization

The content of Mo, Cu, Ni and C species in the passivated catalysts estimated by ICP-OES and elemental analysis is reported on **Table 1**. The C/Mo molar ratio found for the catalysts is between 0.36 and 0.45, which is lower than expected (0.5) considering the chemical formula of the Mo carbide (Mo_2C). This might indicate that the carbon was not effectively incorporated in the Mo structure during carburization.

Table 1 also shows the textural properties of the support and passivated catalysts determined by N_2 physisorption. A decrease in the specific surface area (SSA) and pore volume (P_v) was observed after the synthesis of supported carbides compared to the bare support, consistent with the impregnation of 26 wt. % MoO_3 , which is a nonporous oxide with very low surface area. The N_2 adsorption-desorption isotherms are displayed in **Fig. S1**. All supported catalysts showed a profile similar to that of bare SiO_2 , which according to IUPAC classification corresponds to a type II isotherm, with an H1 hysteresis loop commonly obtained for materials consisting of agglomerates or compacts of approximately uniform spheres [62,63].

Table 1. Chemical composition, textural properties of the support and passivated catalysts.

Material	Content (wt. %)					SSA ^a (m^2/g) ^a	P_v^b (cm^3/g)
	Mo	C	Ni	Cu	active phase		
SiO_2	-	-	-	-	-	198	1.13
$\beta\text{-Mo}_2\text{C}$	-	-	-	-	-	13	0.00
$\beta\text{-Mo}_2\text{C}/\text{SiO}_2$	17.6	0.8	-	-	18.4	140	0.53
$\text{Ni-Mo}_x\text{C}_y/\text{SiO}_2$	16.0	0.9	2.8	-	19.7	142	0.60
$\text{Cu-Mo}_x\text{C}_y/\text{SiO}_2$	14.9	0.8	-	2.0	17.7	137	0.66
Ni/SiO_2	-	-	2.6	-	2.6	187	1.07
Cu/SiO_2	-	-	-	2.1	2.1	185	0.70

^a Determined by BET method

^b Determined by BJH method

Since catalytic testing took place directly after carburization, conventional characterization, for instance by X-ray diffraction (XRD), was not possible. The formation of the supported phases was thus followed by *in situ* XAS, carried out at the Mo, Ni and Cu K-edges, with further input from Raman spectra recorded on the initial treated samples.

The XAS data at the Mo K-edge related to the calcined precursors of Mo₂C/SiO₂, Ni-Mo_xC_y/SiO₂ and Cu-Mo_xC_y/SiO₂ are presented on Figs. S2 - S4. The shape of the XANES spectra and position in energy are similar to those of the MoO₃ standard, especially for Mo₂C/SiO₂ (Fig. S2). For the two promoted catalysts, the only significant difference is the increase of intensity of the second feature after the edge, at 20040 eV, also well visible on a spectrum reported in the literature for γ -CuMoO₄ [64].

Raman spectroscopy confirms that MoO₃ is present on the three samples, (bands at 994, 819 and 665 cm⁻¹ [65], Fig. S5), in a well crystallized form for the precursors of Mo₂C/SiO₂ and Ni-Mo_xC_y/SiO₂, in a more poorly organized form for the precursor of Cu-Mo_xC_y/SiO₂, as evidenced by the low intensity of these bands. It also reveals the existence of a second phase on the oxide precursor of Ni-Mo_xC_y/SiO₂. The weak but well-defined band at 961 cm⁻¹ is unambiguously assigned to α -NiMoO₄ [66,67], a mixed oxide in which octahedral groups of [NiO₆] and [MoO₆] alternate. Some weak bands are also visible for the precursor of Cu-Mo_xC_y/SiO₂. The band at 960 cm⁻¹ may be attributed to CuMoO₄ [68,69], but the broad band at 930 cm⁻¹, which is expected to be thin and poorly intense for crystalline CuMoO₄ [68,69], can rather arise from molybdates with a higher degree of condensation of the molybdate units, such as in Cu₃Mo₂O₉ [70].

The feature at 20040 eV (Fig. S2), the differences of structure of the EXAFS oscillations (Fig. S3) and the differences of shape of the peaks on the associated Fourier transforms for the promoted systems (Fig. S4) are thus linked to the presence of a

mixture of MoO_3 and Ni/Cu molybdates, more crystallized in the case of Ni- $\text{Mo}_x\text{C}_y/\text{SiO}_2$, and less for Cu- $\text{Mo}_x\text{C}_y/\text{SiO}_2$. Due to the complexity of the typical oxidic environment of Mo(VI) ions (several different Mo-O distances ranging between 1.6 and 2.2 Å) and the existence of mixtures in the bimetallic systems, it was not attempted to perform EXAFS fits for the calcined precursors at the Mo K-edge.

Prior to analyzing the carburization process up to 650 °C, the state of Mo after carburization will be investigated here. The XAS analysis was performed on spectra recorded after cooling to room temperature (RT), still under a CH_4/H_2 atmosphere.

After carburization, the XANES spectra, EXAFS oscillations and Fourier transforms of $\text{Mo}_2\text{C}/\text{SiO}_2$, Ni- $\text{Mo}_x\text{C}_y/\text{SiO}_2$ and Cu- $\text{Mo}_x\text{C}_y/\text{SiO}_2$ are very similar, and resemble that of reference bulk $\beta\text{-Mo}_2\text{C}$ (an unsupported sample whose structure was identified by XRD after passivation, and that was reactivated under H_2 at 400 °C before recording the XAS spectrum) (Figs. S6 - S8).

The results of the fits for the first two shells of neighbors (C and Mo atoms) are presented on Figs. 1-2 and in Table 2. They are consistent with the formation of Mo carbides. Given the limited number of independent parameters allowed for the fit, it was chosen to fit each shell with a single contribution of C and Mo. This does not preclude the existence of several interatomic Mo-C or Mo-Mo distances in the structure of the carbide, and a distribution of Mo-C distances can explain the larger error bar for the Debye-Waller parameter obtained by fitting the C shell. It can be added that the possible presence of O atoms in the first shell was always rejected by the fits.

The number of C atoms around Mo is found to be larger in the supported systems than in unsupported $\beta\text{-Mo}_2\text{C}$. However, it must be remembered that the number of neighboring atoms (N) and the Debye-Waller parameter (σ^2) are correlated, and here increase concomitantly. The increase of N(C) can thus be interpreted either as the sign

of a C enrichment around Mo in the carbide, or as an over-estimation of N by the fit, compensating for a high value of σ^2 . A second feature that would allow favoring the hypothesis of a carbon enrichment on the supported systems is linked to the Mo-C and Mo-Mo average interatomic distances, longer by 0.012 to 0.020 Å than those found for the β -Mo₂C standard.

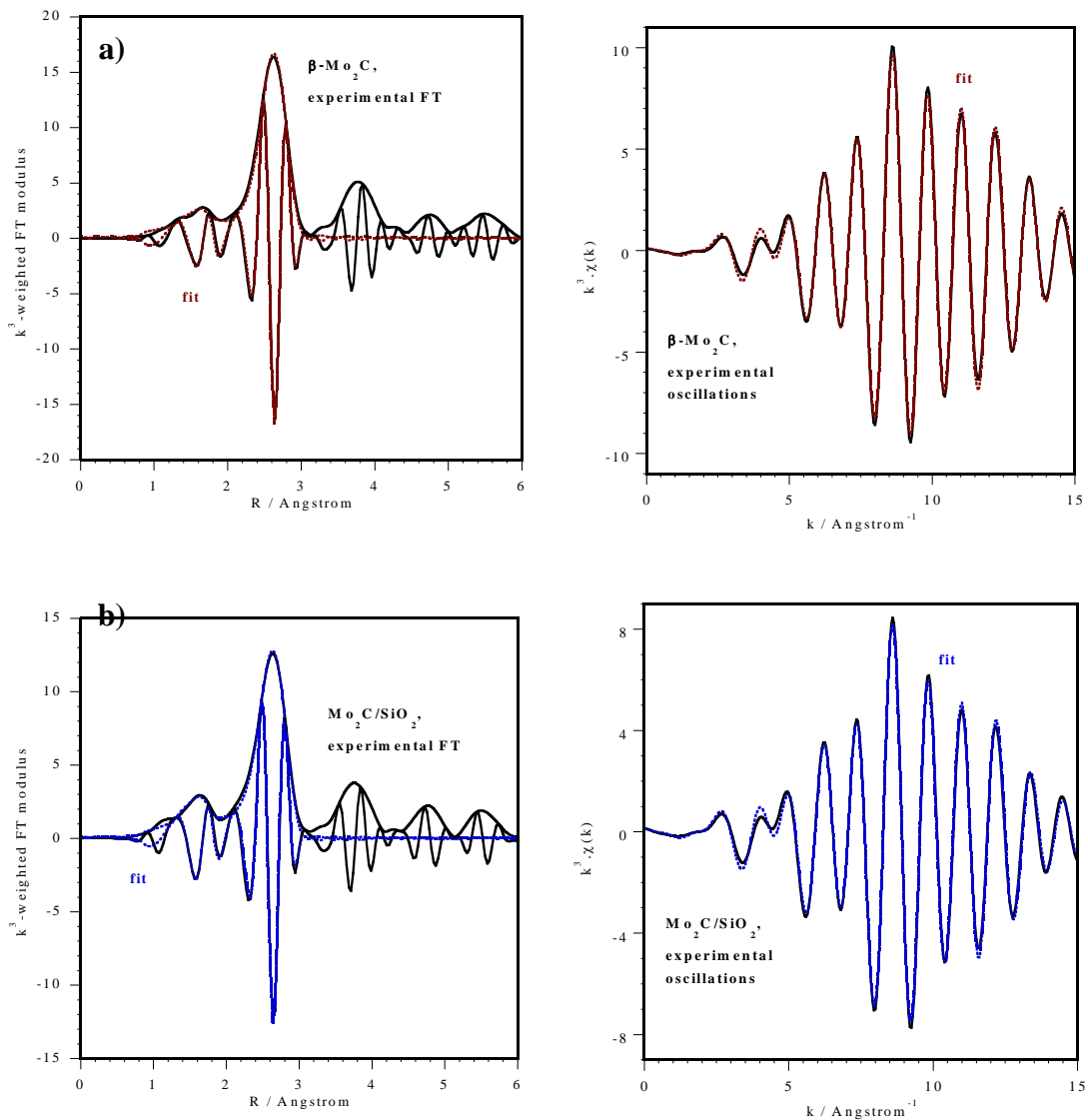


Figure 1. XAS data at the Mo K-edge after carburization of a) β -Mo₂C after reactivation in H₂ at 400 °C, and b) Mo₂C/SiO₂ (spectra recorded at room temperature).

Fit of the first and second shells of neighbors: Fourier transform (left) and EXAFS oscillations (right). $k = 3.5 - 15 \text{ \AA}^{-1}$.

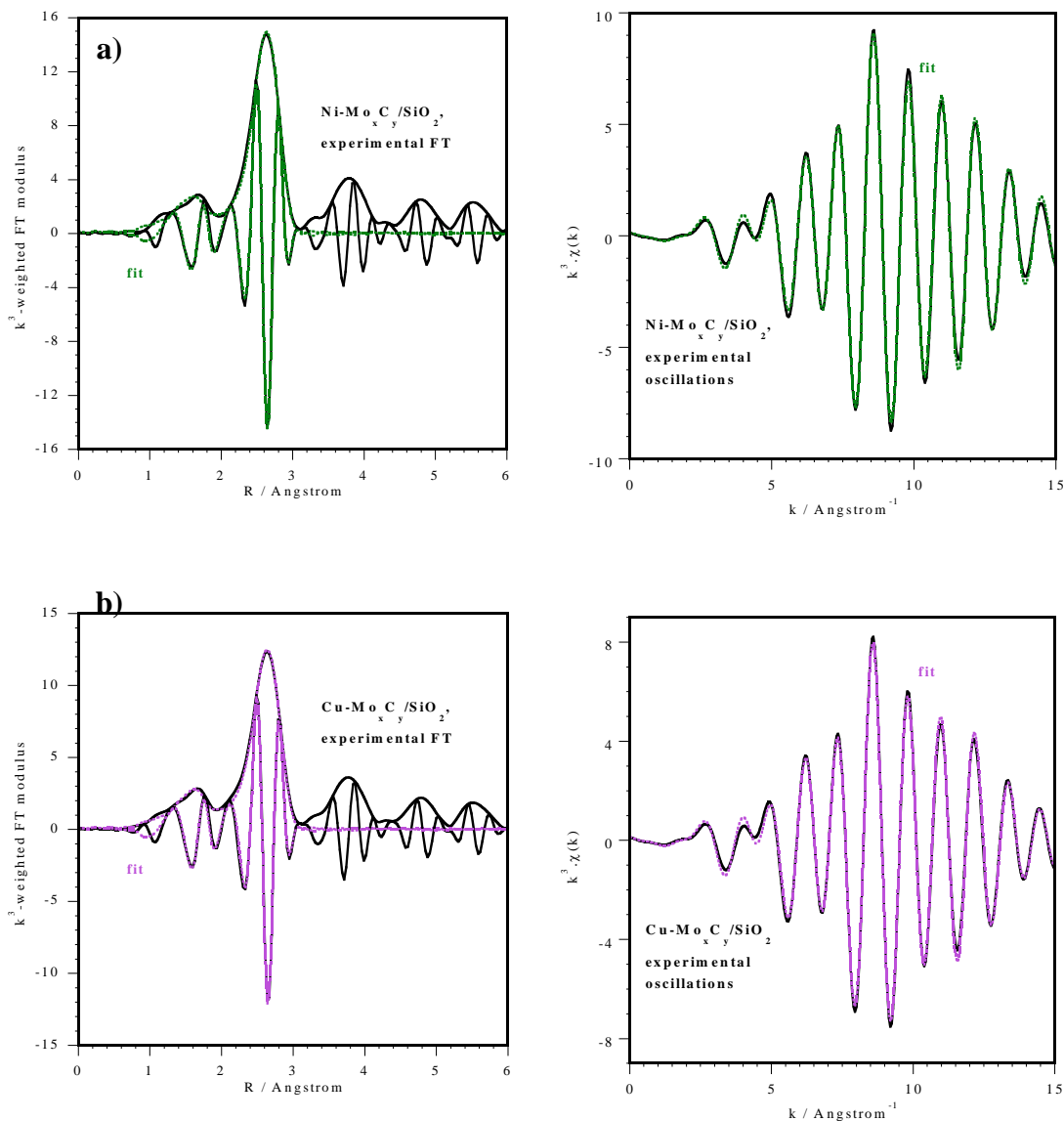


Figure 2. XAS data at the Mo K-edge after carburization of a) Ni-Mo_xC_y/SiO₂ and b) Cu-Mo_xC_y/SiO₂ (spectra recorded at room temperature). Fit of the first and second shells of neighbors: Fourier transform (left) and EXAFS oscillations (right). $k = 3.5 - 15 \text{ \AA}^{-1}$.

Table 2. Fitted parameters at the Mo K-edge ($E_0 = 20013$ eV, $S_0^2 = 0.98$) determined from the EXAFS analysis of spectra recorded at room temperature on carburized catalysts. $k = 3.5 - 15 \text{ \AA}^{-1}$. Fit of the first peaks from the Fourier transform between 1 and 3 \AA .

Catalyst	Backscatter	N	$\sigma^2 (\text{\AA}^2) \times 10^3$	R (\AA)
$\beta\text{-Mo}_2\text{C}^a$	C	2.7 ± 0.9	4.1 ± 0.3	2.08 ± 0.02
	Mo	7.3 ± 0.8	5.7 ± 0.5	2.966 ± 0.005
$\Delta E_0 = -5.5$ eV, r-factor = 0.01575, $\chi^2 = 592$, $N_{\text{ind}} = 13$, $N_{\text{var}} = 7$				
$\beta\text{-Mo}_2\text{C}/\text{SiO}_2$	C	3.5 ± 0.9	6 ± 2	2.10 ± 0.01
	Mo	7.3 ± 0.8	7.3 ± 0.6	2.978 ± 0.005
$\Delta E_0 = -3.8$ eV, r-factor = 0.01462, $\chi^2 = 441$, $N_{\text{ind}} = 13$, $N_{\text{var}} = 7$				
$\text{Ni-Mo}_x\text{C}_y/\text{SiO}_2$	C	4 ± 1	6 ± 2	2.10 ± 0.01
	Mo	7.5 ± 0.8	6.7 ± 0.5	2.979 ± 0.004
$\Delta E_0 = -4.5$ eV, r-factor = 0.01232, $\chi^2 = 301$, $N_{\text{ind}} = 13$, $N_{\text{var}} = 7$				
$\text{Cu-Mo}_x\text{C}_y/\text{SiO}_2$	C	3.5 ± 0.9	6 ± 2	2.10 ± 0.01
	Mo	7.1 ± 0.8	7.2 ± 0.6	2.981 ± 0.005
$\Delta E_0 = -4.2$ eV, r-factor = 0.01481, $\chi^2 = 425$, $N_{\text{ind}} = 13$, $N_{\text{var}} = 7$				

a (after reactivation in H_2 at 400 $^\circ\text{C}$)

The evolution of the XAS spectra at the Mo K-edge during carburization is presented on **Figs. S9 - S11**. The color gradient from blue to red is related to the increase of temperature, from 30 to 650 $^\circ\text{C}$. It is clearly seen that molybdenum is transformed almost continuously during the temperature ramp under CH_4/H_2 , till the Mo carbide is ultimately formed. Qualitatively speaking, one can observe that the first strong shift of the spectra to lower energies (first stage of Mo reduction), along with the appearance of a poorly intense white line at 20020 eV, occurs in a lower temperature

range for Cu-Mo_xC_y/SiO₂ (light blue color) than for Mo₂C/SiO₂ and Ni-Mo_xC_y/SiO₂ (green color).

An analysis of the evolution of Mo speciation was carried out using an MCR-ALS procedure. Each experimental spectrum in the series is considered to be a linear combination of a set of independent, successive spectral components, and the MCR-ALS algorithm extracts both the matrix of spectral components and a matrix of associated “concentrations” evolving with the rising temperature. The spectral components are analyzed using the XAS toolbox, in order to identify the chemical species (if the spectral component is characteristic of a known species), or, as will also be the case here, to obtain spectroscopic or structural footprints of the successive species involved in the carburization process (if the spectral component cannot be associated with a recognizable chemical species, or corresponds to a mixture).

The MCR-ALS procedure could evidence four distinct spectral components in each of the three carburization processes. The first of them corresponds to the spectrum of the initial, calcined precursor (Fig. S12), representing MoO₃ for Mo₂C/SiO₂, and a mixture of MoO₃ and Ni/Cu-Mo(VI) molybdates for Ni-Mo_xC_y/SiO₂ and Cu-Mo_xC_y/SiO₂. This component will be denoted as representing “Mo(VI) oxides” collectively.

For the three samples, the second spectral component (Fig. S13) is characterized by a significant shift of the edge toward lower energies compared with MoO₃, implying a decrease of the average oxidation state of Mo. This shift can be better observed when plotting the derivative of the absorbance as a function of the energy (Fig. S13b). However, the spectral components for the promoted systems differ from that extracted for Mo₂C/SiO₂. The latter still presents a pre-edge (Fig. S13a), as is also seen on the spectrum reported in the literature for Mo₄O₁₁, an oxide in which two Mo atoms have

been reduced to Mo(V) [71]. The position of the maximum of the derivative (Fig. S13b) is indeed intermediate between those of the MoO₃ and MoO₂ standards. In contrast, the derivatives calculated for Ni-Mo_xC_y/SiO₂ and Cu-Mo_xC_y/SiO₂ resemble more that of Mo(IV)-containing MoO₂, in line with the position of the first three EXAFS oscillations (Fig. S13c), and with the position of the peaks on the Fourier transform (Fig. S13d). The second spectral component thus reflects the formation of Mo suboxides (average oxidation state comprised between Mo(IV) and Mo(V) by reduction of Mo(VI)).

The third spectral components (Fig. S14) share two common characteristics: the shape of the XANES spectrum, displaying on the white line a first feature more intense than the second one, similar to the spectra recently assigned to a Mo oxycarbide intermediate [72,73] (Fig. S14a); and a further decrease of the average oxidation state of Mo, with one maximum of the derivative of the XANES spectrum remaining close to that of MoO₂, and a shoulder at a lower energy close to that of metallic Mo (Fig. S14b). This composite aspect is also found in the examination of the EXAFS oscillations. The position of the first oscillations roughly corresponds to those found for MoO₂, but the next ones are clearly different (Fig. S14c). Finally, if the first peak in the Fourier transform is found at the position expected for a O shell, like in MoO₂, the second peak does not correspond to the Mo shell from MoO₂, and is located at a slightly larger distance than the first peak of Mo neighbors in metallic Mo (Fig. S14d).

In order to obtain more precise structural information on these intermediate species, the second and third spectral components extracted for Cu-Mo_xC_y/SiO₂ were selected for EXAFS fitting. This system was chosen because it is the one for which the intermediate phases appear in the most sequential way, and are more likely to represent distinct species.

The identification of a MoO₂-like phase is confirmed for the second spectral component, by comparison with a fit done on the spectrum of MoO₂ using the same number of parameters (Table S1, Fig. S15). The only difference is a Mo-Mo interatomic distance longer by 0.07 Å.

A precise assignment is more difficult to establish for the third spectral component (Table S1, Fig. S16). The first peak in the Fourier transform is found to arise from a shell of O atoms. A fit using both C and O atoms appears as less plausible, because it results in an extremely low Debye-Waller parameter, lower than that found when fitting the EXAFS signal of a well-organized oxide like MoO₂ at RT. The second peak corresponds to Mo neighbors at an interatomic distance of 2.80 Å, which is both larger than the Mo-Mo distance in metallic Mo (2.72 Å), and smaller than the distances evaluated in the carburized catalysts (Table 2; approximately 2.97 Å), or in the crystalline oxycarbide phases whose structure was described in detail by Bouchy *et al.* [74] (2.90 - 2.96 Å). The high Debye-Waller factor for the second shell can be explained by a thermal effect (as will be seen below, the third component is prominent at about 400 °C) or by a structural disorder around Mo.

As a conclusion, a comparison with the spectra presented in the literature points to phases mentioned as oxycarbides MoO_xC_y. But the impossibility to fit the first shell with a combination of C and O atoms, and the Mo-Mo interatomic distance, which significantly differs from those reported either in organized oxycarbide crystals or in metallic Mo, also suggest the formation of a heterogeneous, mostly oxidic, system, in which only a fraction of Mo has pursued its reduction, or is initiating its carburization. It will be seen in the section dedicated to temperature programmed carburization that the degree of carburization of this species may not be the same for the three systems.

Finally, the fourth spectral component extracted by the MCR-ALS procedure is identical to that of the final Mo carbide, as confirmed by comparison of the position of the oscillations with those recorded after cooling under CH₄/H₂ to RT (Fig. S17). The damping is due to thermal effects.

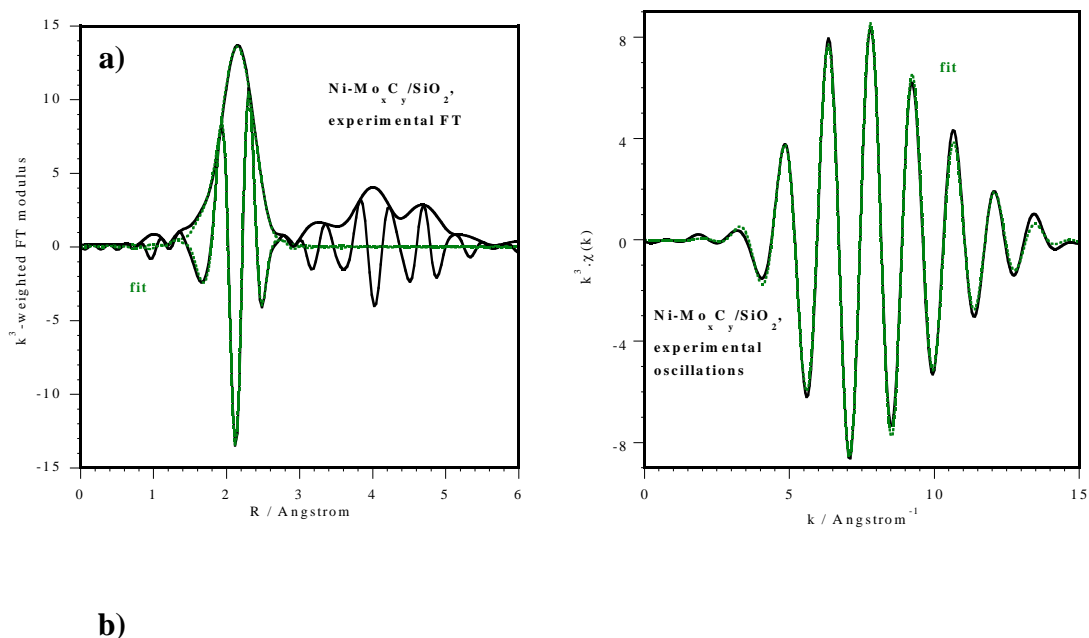
The evolution of the spectra recorded during carburization of Ni-Mo_xC_y/SiO₂ at the Ni K-edge is presented on Fig. S18. The initial intense white line is characteristic of Ni²⁺, and its disappearance indicates that nickel is reduced to the metallic state during the first half of the ramp. But even after reduction, some changes in the spectra are visible (yellow-red spectra).

EXAFS confirms that in the calcined precursor, Ni²⁺ is present in the α-NiMoO₄ phase detected by Raman spectroscopy; NiO would provide very different oscillations (Fig. S19). The expected number of neighbors and interatomic distances in the crystal structure are 6 O atoms at R = 2.018 - 2.140 Å, 2 Ni atoms at R = 3.027 Å, and 2 Mo atoms at R = 3.207 Å, and correspond to those determined by fitting (Table 3). The fit was not attempted at longer distances owing to the superimposition of more than 10 multiple scattering paths between 3.4 and 4 Å.

A spectrum recorded during carburization at 400 °C is presented on Fig. S20a. As was anticipated from Fig. S18, Ni is now in a reduced, metallic state (comparison of the edge position with Ni foil, position in energy of the main oscillations, Fig. S20a and b). But the shape of the spectrum just past the edge is quite different from that of bulk Ni metal, with a complete absence of structuration around 8350 eV. The peak of nearest neighbors on the Fourier transform is also located at a significantly shorter distance than in metallic Ni (Fig. S20c), which may indicate that small groups of Ni atoms, which one can presume are stabilized by an underlying phase, have not formed yet well-organized metal particles.

In contrast, after carburization has been completed and cooling to RT has taken place (Fig. 3a and S21), face-centered (fcc) cubic Ni is clearly detected. The number of nearest neighbors is far below the value of 12 in bulk Ni (Table 3). A value of 6.8, as found here, can be linked to small Ni particles, whose size would be close to 1 nm [75], a highly dispersed state for reduced Ni. The interatomic distance (2.494 Å) corresponds to that in metallic Ni, and the hypothesis of a Ni carbide, in which distances are longer, can be excluded (a Ni - Ni distance of 2.63 Å was reported for Ni₃C by Struis *et al.* [76]).

The MCR-ALS analysis of the carburization of Ni-Mo/SiO₂ at the Ni K-edge extracts three spectral components (Figs. S22 - 24). The first one corresponds to NiMoO₄, the second one is identical to the spectrum recorded at 400 °C (small groups of Ni atoms), the third one to fcc Ni nanoparticles, with EXAFS oscillations damped because of a strong thermal effect in the last part of the temperature ramp.



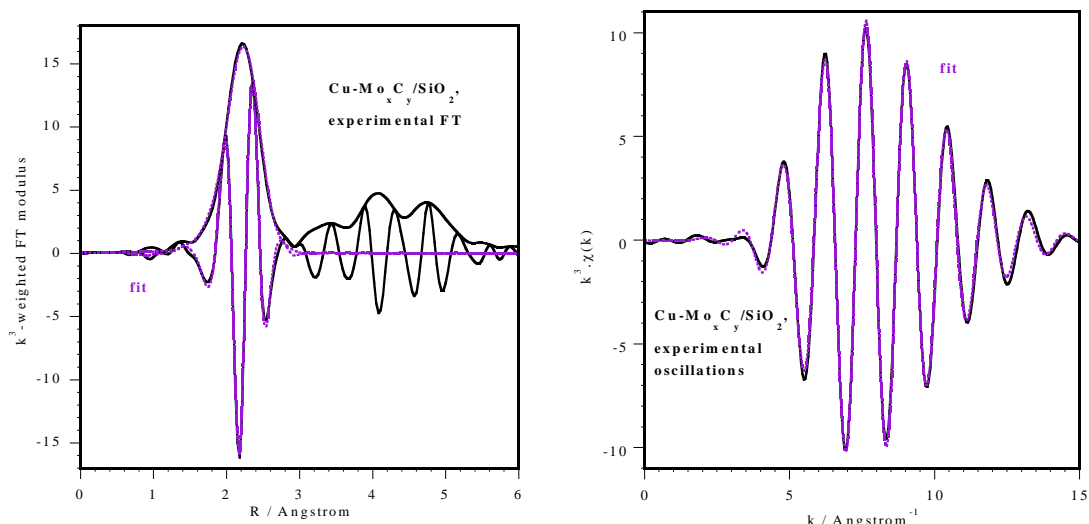


Figure 3. XAS data a) of Ni-Mo_xC_y/SiO₂ at the Ni K-edge and b) of Cu-Mo_xC_y/SiO₂ at the Cu K-edge, after carburization (spectra recorded at room temperature). Fit of the first shell of neighbors: Fourier transform (left) and EXAFS oscillations (right), $k = 3 - 13 \text{ \AA}^{-1}$ at the Ni K-edge, $k = 3.5 - 14 \text{ \AA}^{-1}$ at the Cu K-edge.

Table 3. Fitted parameters at the Ni K-edge ($E_0 = 8339 \pm 2 \text{ eV}$, $S_0^2 = 0.80$) or at the Cu K-edge ($E_0 = 8987 \pm 4 \text{ eV}$, $S_0^2 = 0.91$) determined from the EXAFS analysis of spectra recorded at room temperature. $k = 3 - 13 \text{ \AA}^{-1}$ at the Ni K-edge, $k = 3.5 - 14 \text{ \AA}^{-1}$ at the Cu K-edge. Fit of the first peak(s) from the Fourier transform between 1 and 3 \AA .

Catalyst	Backscatterer	N	$\sigma^2 (\text{\AA}^2) \times 10^3$	R (\AA)
Ni-Mo _x C _y /SiO ₂ calcined	O	6.4 ± 0.7	6 ± 2	2.030 ± 0.009
	Ni	1.4 ± 0.6	6 ± 2	2.97 ± 0.03
	Mo	1.6 ± 0.9	6 ± 2	3.17 ± 0.03
r-factor = 0.01766, $\chi^2 = 365$, $N_{\text{ind}} = 12$, $N_{\text{var}} = 8$				
Ni-Mo _x C _y /SiO ₂ carburized	Ni	6.8 ± 0.5	8.3 ± 0.6	2.494 ± 0.004
	r-factor = 0.00473, $\chi^2 = 427$, $N_{\text{ind}} = 12$, $N_{\text{var}} = 4$			
Cu-Mo _x C _y /SiO ₂ calcined	O	4.9 ± 0.3	4.9 ± 0.6	1.941 ± 0.004
	r-factor = 0.00791, $\chi^2 = 41$, $N_{\text{ind}} = 13$, $N_{\text{var}} = 4$			
Cu-Mo _x C _y /SiO ₂ carburized	Cu	9.0 ± 0.7	9.6 ± 0.6	2.544 ± 0.005
	r-factor = 0.00598, $\chi^2 = 148$, $N_{\text{ind}} = 13$, $N_{\text{var}} = 4$			

The evolution of the spectra recorded during carburization of Cu-Mo_xC_y/SiO₂ at the Cu K-edge is presented on Fig. S25. The reduction of Cu²⁺, characterized by the intense white line, takes place at a low temperature. An intermediate species then contributes to a well-visible pre-edge feature, distinct from that of metallic Cu and more intense, before the typical spectrum of metallic Cu appears.

The analysis of the XAS data is much less informative than at the Ni K-edge. The position in energy of the XANES spectrum recorded on the calcined system (Fig. S26) is similar to that of standard CuO, which indicates that Cu is present in the Cu²⁺ state, but the spectrum is different: for example, no pre-edge feature is present. This absence of a pre-edge feature was also reported in the literature for γ -CuMoO₄ [64]. The fit of the EXAFS data only reveals a shell of O atoms around Cu²⁺, which explains why the EXAFS oscillations are seen at approximately the same energies as in CuO (Table 3). These observations remain consistent with the hypothesis of poorly organized Cu²⁺ molybdates suggested by Raman spectroscopy.

Fig. S27 presents two spectra recorded at 200 and 240 °C. At 200 °C, the position of the edge is intermediate between that of CuO and Cu₂O. However, the intense pre-edge feature and the EXAFS oscillations are quite different from those of these standards. In contrast, the species detected at 240 °C is clearly metallic Cu. This is confirmed by the Fourier transform that shows the four successive peaks characteristic of the face-centered cubic metal (Fig. S28). At 200 °C, the Fourier transform presents two peaks: one at the position of O nearest-neighbors, like in Cu₂O; the second one at the position of Cu nearest-neighbors in the metal, and not in Cu₂O. XANES spectra found in the literature that display the same shape have been interpreted either as Cu₂O clusters, small partly oxidized Cu clusters, or metallic Cu clusters stabilized by ligands

or by an oxidic matrix [77–85](Bazin, 1997). The position of the peaks on the Fourier transform favors the latter interpretation.

After carburization and cooling to RT, Cu is unambiguously present as fcc Cu nanoparticles (Fig. 3b and S29). The number of nearest neighbors, 9 (Table 3), shows that these nanoparticles are larger than the Ni nanoparticles detected after carburization of Ni-Mo_xC_y/SiO₂.

The MCR-ALS analysis of the carburization ramp at the Cu K-edge provides four spectral components (Figs. S30 - 33): Cu²⁺ in the initial copper molybdates; the Cu clusters in contact with an oxidic matrix; metallic fcc Cu nanoparticles; and a fourth component also representing metallic Cu (XANES spectrum), but whose Fourier transform is shifted to lower distances compared with the metal standard. Spectra recorded during the cooling of the sample shows that this contribution reverts back to the third spectral component in a linear way with respect to temperature. One can thus surmise that the fourth contribution comes from a reversible thermally-induced distortion of the spectrum of Cu nanoparticles. The third and fourth contribution will thus be treated as a single species, fcc Cu, in the following.

The reduction of Mo oxides and the formation of Mo carbides during carburization with CH₄ and H₂ mixture was followed by temperature programmed carburization in a parallel experiment (Fig. 4), which revealed the associated production of water and CO.

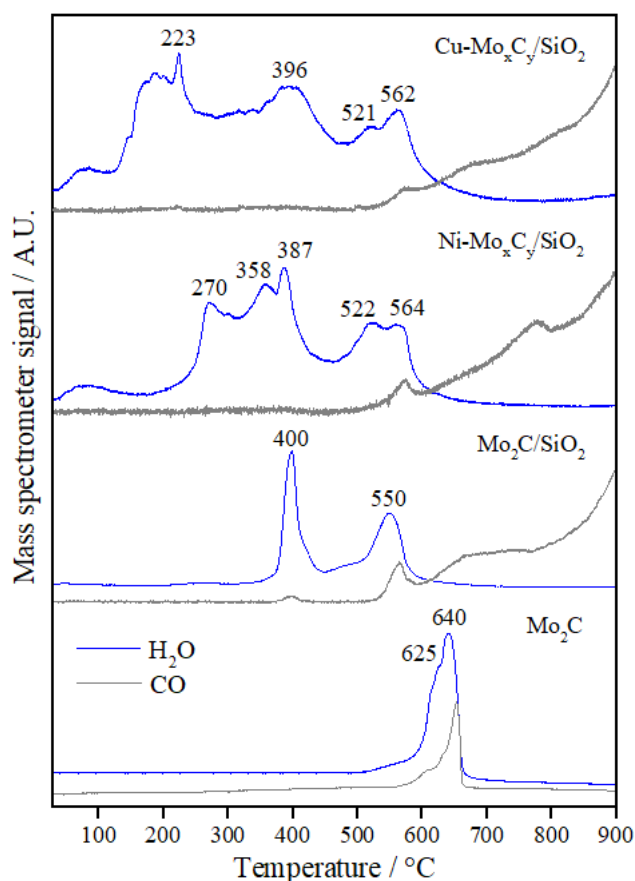
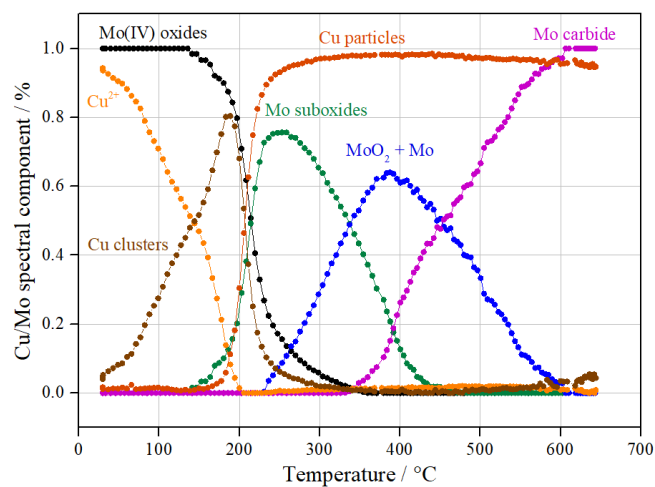


Figure 4. Water and CO formation profiles during temperature programmed carburation of the calcined precursors of Cu-Mo_xC_y/SiO₂, Ni-Mo_xC_y/SiO₂, Mo₂C/SiO₂ and Mo₂C.

The water signal during the carburization of the unsupported Mo₂C catalyst showed a maximum at 640 °C with a shoulder at 625 °C (Fig. 4). According to the literature, for the MoO₃ carburization taking place in an atmosphere of CH₄/H₂, the latter peak is ascribed to the reduction of MoO₃ to MoO₂, while the former corresponds to the carburization of MoO₂ and formation of the Mo carbide (β-Mo₂C), which is followed by the consumption of methane and production of CO [45,86–88].

The thermograms of the supported catalysts, in special the bimetallic carbides, are way more complex and difficult to interpret, but the MCR-ALS analysis of the *in situ* XAS experiments sheds light on the changes of Mo, Ni and Cu speciation taking place during the ramp. The weights of each spectral component deduced from the MCR-ALS

analysis are presented as a function of temperature on Fig. 5. Each curve corresponding to the disappearance of a species, by reduction or carburization, exhibits an inflection point (maximum rate of consumption), that should correspond to a peak of water or CO production on the thermograms, allowing identification of the various stages of reaction.



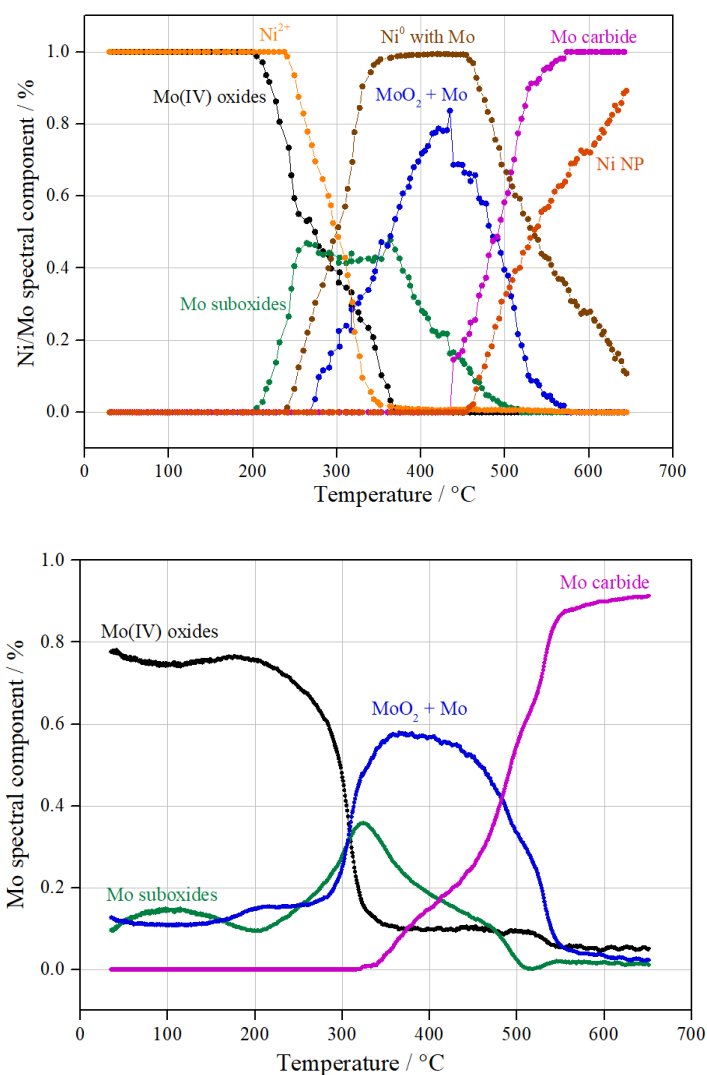


Figure 5. Concentrations profiles of Mo, Ni and Cu species during TPC of the calcined precursors of a) Cu-Mo_xC_y/SiO₂, b) Ni-Mo_xC_y/SiO₂ and c) Mo₂C/SiO₂ from MCR-ALS analysis of the Mo, Ni and Cu K-edge data.

By supporting the carbide on silica (Mo₂C/SiO₂ catalyst), the transformations occur at clearly lower temperatures than for the bulk carbide. The main two peaks are shifted to 400 and 550 °C. XAS suggests that the very small production of water around 300 °C corresponds to the reduction by H₂ of MoO₃ to a Mo suboxide. The very low degree of reduction could validate the hypothesis of a reduction to Mo₄O₁₁, in which the reduction of Mo(VI) to Mo(V) concerns a minor number of Mo ions. Given the overlapping domains of predominance of the second and third components, the exact attribution of

the peak at 400 °C is more difficult. It could be associated to a further reduction of Mo_4O_{11} to the species providing the third spectral component, and a minor concomitant production of CO could be linked to the starting carburization of a Mo fraction. The water production and onset of CO production at 550 °C correspond to the formation of the Mo carbide.

For the $\text{Ni-Mo}_x\text{C}_y/\text{SiO}_2$ catalyst, the peaks at 270 and 358 °C are associated with the reduction of MoO_3 and NiMoO_4 , to groups of reduced Ni atoms and MoO_2 , respectively. The reduction of NiMoO_4 was indeed reported to occur in the 250 - 400 °C range in the literature [89]. Because of the slightly delayed reduction of Ni^{2+} with respect to Mo(VI), which was checked not to be an analysis artefact by comparing the experimental spectra at the Mo and Ni K-edges in the 220 - 250 °C range, NiMoO_4 seems to reduce after the reduction of MoO_3 has started. Compared with $\text{Mo}_2\text{C}/\text{SiO}_2$, there is a significant gain in reduction temperature. The peak at 387 °C can be assigned to the reduction of MoO_2 to the partly reduced oxide represented by the third spectral component. In this case, the reaction is not accompanied by a release of CO and the oxide may not exhibit carburization. As was the case for $\text{Mo}_2\text{C}/\text{SiO}_2$, the final Mo carburization takes place above 500 °C, in two stages that the MCR-ALS analysis cannot explain. It is accompanied by the formation of the fcc Ni nanoparticles (NP).

For the $\text{Cu-Mo}_x\text{C}_y/\text{SiO}_2$ catalyst, the intensity of the water signal starts to increase at 120 °C, and exhibits a maximum at 223 °C with several shoulders. These peaks are associated with the reduction of Cu^{2+} in the copper molybdate phases, followed by the rapid reduction of Mo(VI) oxides to MoO_2 . Compared with the former systems, the gain in temperature for this reduction step is relevant. It may be associated to the poorly crystalline nature of the Cu molybdates and to the subsequent activation of H_2 on the newly-formed Cu nanoparticles in the 200 - 225 °C range. The next pronounced peak at

396 °C refers to the reduction of MoO₂ to the partly reduced oxide represented by the third spectral component, here again without production of CO, and the final stages of carburization take place above 500 °C.

In conclusion, both the TPC profiles and MCR-ALS diagrams indicate that the last steps of reduction and carburization occur in the same temperature range for the three supported catalysts. The main gain upon addition of a promoter concerns the initial reduction of Mo(VI) oxides, and can be linked to the crystallinity of the mixed molybdates, and to the temperature at which metal particles able to activate H₂ are formed.

This effect was observed before by Jung *et al.* [50] during the carburization of MoO₃ promoted with Ni, Cu, Co, Pd, Pt under CH₄/H₂. The presence of a promoter decreased the starting temperature of the initial reduction for all materials. Similarly, Zhang *et al.* [49] observed by temperature programmed reduction of NiO, MoO₃ and NiMoO_x in H₂ that Ni species in NiMoO_x were more difficult to reduce than in NiO, while the Mo species were easily reduced in comparison with MoO₃.

On the other hand, the presence of Ni and Cu as promoters has been reported in the literature to favor the carburization process because this metal causes the activation and dissociation of CH₄ into carbon and hydrogen at lower temperatures compared with non-promoted carbides [46,50], but this is not observed in the present work.

We also demonstrate that after completion of carburization, Ni and Cu are both present as metal nanoparticles, probably in a strong stabilizing interaction with the underlying Mo carbide given their small size, but bimetallic NiMo or CuMo carbide phases were not formed. Ni nanoparticles appear as more dispersed than Cu nanoparticles, and no Ni carbide is evidenced after carburization.

3.2 HDO of m-cresol over Mo carbides-based catalysts

The HDO reaction rate, distribution of products and yield at low conversion using m-cresol as a model molecule are reported in [Table 4](#). Mo₂C, Mo₂C/SiO₂, and Ni-Mo_xC_y/SiO₂ exhibited approximately the same HDO deoxygenation activity whereas Cu-Mo_xC_y/SiO₂ and Ni/SiO₂ were less active (10-fold).

Regarding product distribution, toluene was the only product formed over Mo₂C, Mo₂C/SiO₂, and Cu-Mo_xC_y/SiO₂ catalysts. In addition to toluene, a small amount of m-cyclohexene (4.2 %) was also produced over Ni-Mo_xC_y/SiO₂ catalyst. On the other hand, several products were observed for Ni/SiO₂ catalyst: methane (31.1 %), m-cyclohexanone (32.3 %), toluene (20.2 %), m-cyclohexanol (7.5 %), phenol (7.0 %), and minor amounts of cyclohexanone, benzene and m-cyclohexene. These results reveal that the Mo-carbide phase is quite selective to deoxygenation products.

[Table 5](#) lists the product distribution for the HDO of m-cresol obtained with different catalysts from the literature [\[11,15,19,90\]](#). Ni-based catalyst promotes the hydrogenolysis and the formation of methane as well as the hydrogenation of the ring with the production of m-cyclohexanone and m-cyclohexanol. Pd/SBA-15, Pd/SiO₂ and Pt/SiO₂ are quite selective to m-cyclohexanone without methane formation. Oxophilic metals such as Ru and Fe promote the formation of toluene. Furthermore, the presence of unreduced iron (Lewis acid site) favors the alkylation reaction and the production of xylenols and o-cresol. Therefore, the type of the active phase significantly affects product distribution for the HDO of m-cresol. This has been previously reported in the literature for the HDO of phenol [\[22,23\]](#). Teles *et al.* [\[22\]](#) studied the effect of metal type on HDO of phenol over silica supported catalysts. They suggested that phenol is mainly tautomerized, followed by hydrogenation of the aromatic ring over Pd/SiO₂,

Pt/SiO₂, and Rh/SiO₂ catalysts. Oxophilic metals such as Ru and Co promote the direct deoxygenation to benzene and hydrogenolysis with the production of methane.

The different reaction pathways proposed in the literature for the HDO of m-cresol are represented by [Scheme 1](#) [10,14,19,90]. The results obtained in our work suggest that the Mo-carbide phase promotes the direct deoxygenation to toluene as it is observed for oxophilic metals such as Ru [11]. DFT calculations showed that the direct dehydroxylation of m-cresol is more favorable than the tautomerization route over the more oxophilic Ru (0001) surface. The direct dehydroxylation of m-cresol over Ru (0001) produces a partially unsaturated hydrocarbon surface species C₇H₇*, which may lead to the formation of C₁-C₅ hydrogenolysis products or toluene by its hydrogenation. For Ru/SiO₂ catalyst, the C₁-C₅ hydrocarbons were the main products formed (54.1 %) [11]. In comparison to Ru, Mo₂C phase does not produce methane, which is responsible for its higher formation of toluene. This result suggests that Mo₂C phase promotes the hydrogenation of the unsaturated hydrocarbon surface species C₇H₇*.

Furthermore, Cu does not exhibit significant activity since the product distribution of Cu-Mo_xC_y/SiO₂ was exactly the same of that observed for Mo₂C/SiO₂. In the case of Ni-Mo_xC_y/SiO₂ catalyst, the presence of isolated metallic Ni particles is evidenced by the formation of methyl-cyclohexene. According to the reaction pathways of [Scheme 1](#), methylcyclohexanone is hydrogenated to methylcyclohexanol, followed by dehydration to methylcyclohexene. Methylcyclohexanone was one of the main products formed over Ni/SiO₂ catalyst. This result is in agreement with the XAS results that demonstrated the presence of isolated metallic Ni particles and Mo₂C phase. In addition, this result also shows that a bimetallic Ni-Mo carbide phase was not formed.

The high content of Ni (10 wt. %) in a bimetallic Mo carbide supported on mesoporous silica (NiMo₂C/SBA-15) also led to the formation of ring hydrogenation

products (methylcyclohexane, methylcyclohexanol, methylcyclohexene) in the HDO of m-cresol at 250 °C and 20 bar of H₂. As in our case, no bimetallic Ni-Mo carbide was formed and Ni was found in its metallic form. Although the catalyst contained 10 wt. % of Mo₂C, no toluene was produced and the C=C hydrogenation was the preferential route [33].

These results confirm that the Mo carbide is the active phase responsible to perform the deoxygenation of m-cresol. An almost complete selectivity to toluene was obtained at atmospheric pressure using Mo₂C as catalyst at high and low conversions of m-cresol achieved by varying the temperature between 150 and 210 °C [34]. In fact, the high selectivity of Mo carbides to perform the direct deoxygenation route has been observed previously for other phenolic compounds. This pathway was dominant on the HDO of p-cresol, when using Mo₂C supported on activated charcoal [32] or over both unsupported Mo₂C and W₂C catalysts in the HDO of anisole at 150 °C and atmospheric pressure, which produced benzene as the main product [37].

The superior ability of the carbides to perform deoxygenation was also demonstrated comparing the catalytic performance of a Mo carbide supported on activated carbon to noble metal-based catalysts (Ru and Pd) for the HDO of guaiacol at 330 °C and 34 bar of H₂. The catalytic results showed that the reaction initially proceeds by the hydrogenation of the phenyl ring of guaiacol over Ru and Pd, while only deoxygenated products such as phenol, 2-methylphenol and 4-methylphenol were observed over the Mo₂C catalyst, indicating that this catalyst does not tend to generate ring saturation products. The main disadvantage of the carbide with respect to the noble metals catalysts, however, was a lower reaction rate [43].

Table 4. Conversion, HDO reaction rate and selectivity for the HDO of m-cresol over Mo carbides catalysts at 300 °C and 1 atm.

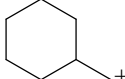
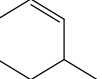
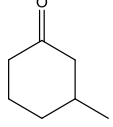
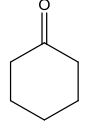
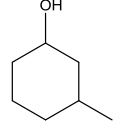
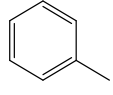
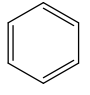
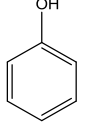
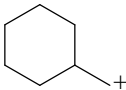
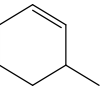
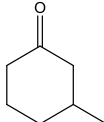
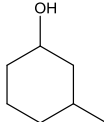
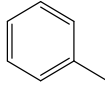
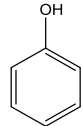
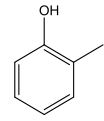
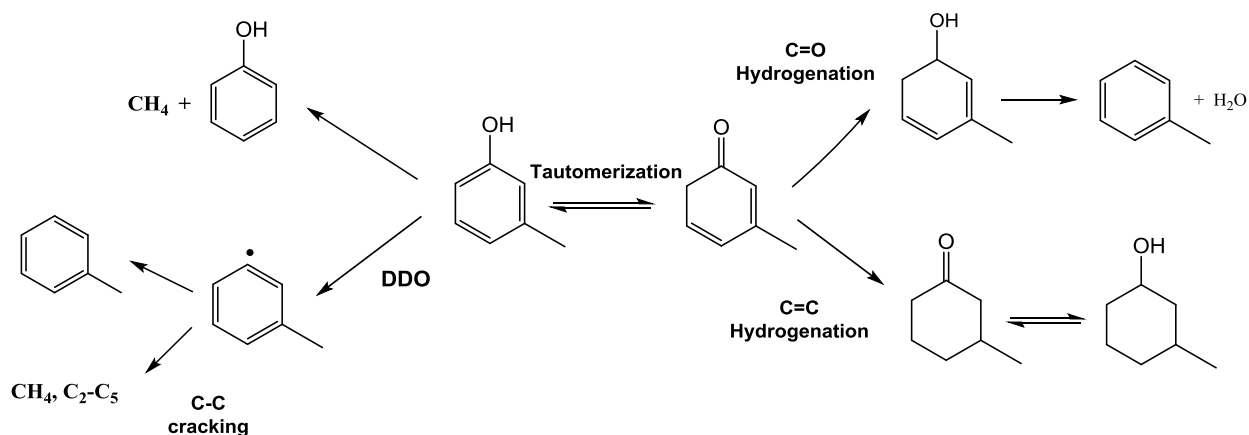
Catalyst	Conversion (%)	Rate of HDO (mmol g ⁻¹ min ⁻¹)	Selectivity (%)								
			CH ₄								
Mo ₂ C	14.9	0.38	-	-	-	-	-	-	100.0	-	-
Mo ₂ C/SiO ₂	17.1	0.25	-	-	-	-	-	-	100.0	-	-
Ni-Mo _x C _y /SiO ₂	22.7	0.32	-	4.2	-	-	-	-	95.8	-	-
Cu-Mo _x C _y /SiO ₂	8.7	0.04	-	-	-	-	-	-	100.0	-	-
Ni/SiO ₂	17.7	0.05	-	0.2	32.3	1.0	7.5	20.2	0.4	7.0	

Table 5. Conversion and distribution of products for the HDO of m-cresol over different catalysts from the literature at 300 °C and 1 atm.

Catalyst	Conversion (%)	Selectivity (%)								Reference
		CH ₄								
5 % Ni/SiO ₂	16.2	13.0	-	33.3	11.1	14.2	-	28.4	-	[19]
5 % Fe/SiO ₂	8.8	-	-	-	-	60.2	-	39.8	-	[19]
5 % Ni-5 % Fe/SiO ₂	13.7	2.2	-	-	-	52.6	-	45.3	-	[19]
Pt/SiO ₂	7.2	-	-	60.2	6.5	33.3	-	-	-	[20]
Ru/SiO ₂	4.5	43.4 (10.7) ^a	-	7.4	-	38.5	-	-	-	[20]
Pd/SBA-15	7.0	-	-	62.0	-	38.0	-	-	-	[15]
Pd/5 % Al-SBA-15	5.0	-	--	5.0	--	77.0	3.0	9.0	6.0	[15]
Pd/20 % Al-SBA-15	6.0	--	--	--	--	50.0	8.0	27.0	15.0	[15]
Pd/SiO ₂	8.2	--	0.0	90.3	5.9	3.8	--	--	--	[90]
Pd/CeO ₂	11.5	--	0.0	78.4	9.9	11.7	--	--	--	[90]
Pd/ZrO ₂	14.7	--	0.4	18.4	1.2	80.0	--	--	--	[90]
Pd/TiO ₂	7.3	--	0.0	12.6	0.0	87.9	--	--	--	[90]
Pd/Nb ₂ O ₅	13.1	--	0.6	3.8	0.0	95.6	--	--	--	[90]

^aC₂-C₅ hydrocarbons



Scheme 1. Reaction scheme for the HDO of m-cresol.

4. Conclusions

The carburization of a monometallic ($\text{Mo}_2\text{C}/\text{SiO}_2$) and bimetallic Mo carbides ($\text{Ni-Mo}_x\text{C}_y/\text{SiO}_2$ and $\text{Cu-Mo}_x\text{C}_y/\text{SiO}_2$) under a CH_4/H_2 mixture was investigated by *in situ* XAS. The synthesis of the monometallic carbide proceeded by reduction of the calcined precursor MoO_3 in the range of 300 and 400 °C, while the final carbide is formed above 500 °C.

Regarding the bimetallic carbides, the results showed that the reduction of the Cu species (molybdates) in the $\text{Cu-Mo}_x\text{C}_y/\text{SiO}_2$ catalyst started at lower temperatures in comparison with Mo species in the monometallic carbide. The produced Cu metallic particles assisted the initial reduction of the Mo species in the Cu-promoted Mo carbide by providing more hydrogen.

On the other hand, Ni species in the $\text{Ni-Mo}_x\text{C}_y/\text{SiO}_2$ catalyst were reduced at higher temperatures than the Mo species and did not contribute to the first step of reduction. No bimetallic NiMo or CuMo carbide phases were formed and Ni and Cu were found only as nanoparticles in contact with the carbide phase. Finally, both metals did not

assist the formation of the Mo carbide at higher temperatures, which occurred at the same range of temperature as observed for the monometallic Mo₂C/SiO₂ catalyst.

An unsupported and the SiO₂-supported Mo carbides were evaluated for the HDO of m-cresol in gas phase at 300 °C and ambient pressure. With exception of the Cu-Mo_xC_y/SiO₂ catalyst, all Mo carbides showed similar deoxygenation activity exhibiting high yields to toluene (> 96 %). Only a lower formation of toluene was observed for the Mo carbide promoted with Ni, which also followed the hydrogenation route producing methylcyclohexene due to the presence of Ni metallic particles ascertained by XAS.

The comparison of the catalytic performance of the Mo carbides with noble-metal based catalysts in the literature under iso-conversion of m-cresol proved the high selectivity of carbides to promote the formation of deoxygenated compounds.

Acknowledgments

Leticia F. Sosa thanks Coordenação de Aperfeiçoamento de Pessoal de Ensino Superior (CAPES - Finance code 001) and CAPES – COFECUB program (88881.142911/2017-01) for the scholarship. This study was supported by the French government through the Programme Investissement d'Avenir (I-SITE ULNE / ANR-16-IDEX-0004 ULNE) managed by the Agence Nationale de la Recherche, CNRS, Métropole Européen de Lille (MEL) and Region Hauts-de-France for “CatBioInnov” project are also acknowledged. Fabio B. Noronha thanks Fundação de Amparo à Pesquisa do Estado do Rio de Janeiro (FAPERJ – E-26/202.783/2017; 200.966/2021) and Conselho Nacional de Desenvolvimento Científico e Tecnológico (CNPq - 303667/2018-4; 305046/2015-2; 302469/2020-6; 310116/2019-82) for financial support. **Acknowledgments to Soleil and grant number**

References

- [1] J.A. Okolie, S. Nanda, A.K. Dalai, J.A. Kozinski, *Chemistry and Specialty Industrial Applications of Lignocellulosic Biomass, Waste Biomass Valor.* 12 (2021) 2145–2169. <https://doi.org/10.1007/s12649-020-01123-0>.
- [2] Y. Liu, Y. Nie, X. Lu, X. Zhang, H. He, F. Pan, L. Zhou, X. Liu, X. Ji, S. Zhang, Cascade utilization of lignocellulosic biomass to high-value products, *Green Chem.* 21 (2019) 3499–3535. <https://doi.org/10.1039/C9GC00473D>.
- [3] D.A. Ruddy, J.A. Schaidle, J.R. Ferrell III, J. Wang, L. Moens, J.E. Hensley, Recent advances in heterogeneous catalysts for bio-oil upgrading via “ex situ catalytic fast pyrolysis”: catalyst development through the study of model compounds, *Green Chem.* 16 (2014) 454–490. <https://doi.org/10.1039/C3GC41354C>.
- [4] J. Zhang, J. Sun, Y. Wang, Recent advances in the selective catalytic hydrodeoxygenation of lignin-derived oxygenates to arenes, *Green Chem.* 22 (2020) 1072–1098. <https://doi.org/10.1039/C9GC02762A>.
- [5] R. Shu, R. Li, B. Lin, C. Wang, Z. Cheng, Y. Chen, A review on the catalytic hydrodeoxygenation of lignin-derived phenolic compounds and the conversion of raw lignin to hydrocarbon liquid fuels, *Biomass and Bioenergy.* 132 (2020) 105432. <https://doi.org/10.1016/j.biombioe.2019.105432>.
- [6] P.M. de Souza, R.C. Rabelo-Neto, L.E.P. Borges, G. Jacobs, B.H. Davis, U.M. Graham, D.E. Resasco, F.B. Noronha, Effect of Zirconia Morphology on Hydrodeoxygenation of Phenol over Pd/ZrO₂, *ACS Catal.* 5 (2015) 7385–7398. <https://doi.org/10.1021/acscatal.5b01501>.
- [7] A.J.R. Hensley, Y. Wang, J.-S. McEwen, Phenol Deoxygenation Mechanisms on Fe(110) and Pd(111), *ACS Catal.* 5 (2015) 523–536. <https://doi.org/10.1021/cs501403w>.
- [8] C. Newman, X. Zhou, B. Goundie, I.T. Ghampson, R.A. Pollock, Z. Ross, M.C. Wheeler, R.W. Meulenberg, R.N. Austin, B.G. Frederick, Effects of support identity and metal dispersion in supported ruthenium hydrodeoxygenation catalysts, *Applied Catalysis A: General.* 477 (2014) 64–74. <https://doi.org/10.1016/j.apcata.2014.02.030>.
- [9] M.B. Gri, J.A. Schaidle, Role of the Support and Reaction Conditions on the Vapor-Phase Deoxygenation of m-Cresol over Pt/C and Pt/TiO₂ Catalysts, *ACS Catal.* (2016) 13.
- [10] P.M. de Souza, L. Nie, L.E.P. Borges, F.B. Noronha, D.E. Resasco, Role of Oxophilic Supports in the Selective Hydrodeoxygenation of m-Cresol on Pd Catalysts, (n.d.) 7.
- [11] Q. Tan, G. Wang, L. Nie, A. Dinse, C. Buda, J. Shabaker, D.E. Resasco, Different Product Distributions and Mechanistic Aspects of the Hydrodeoxygenation of m-Cresol over Platinum and Ruthenium Catalysts, *ACS Catal.* (2015) 13.
- [12] T.M. Sankaranarayanan, A. Berenguer, C. Ochoa-Hernández, I. Moreno, P. Jana, J.M. Coronado, D.P. Serrano, P. Pizarro, Hydrodeoxygenation of anisole as bio-oil model compound over supported Ni and Co catalysts: Effect of metal and support properties, *Catalysis Today.* 243 (2015) 163–172. <https://doi.org/10.1016/j.cattod.2014.09.004>.
- [13] T.N. Phan, Y.-K. Park, I.-G. Lee, C.H. Ko, Enhancement of C O bond cleavage to afford aromatics in the hydrodeoxygenation of anisole over ruthenium-supporting mesoporous metal oxides, *Applied Catalysis A: General.* 544 (2017) 84–93. <https://doi.org/10.1016/j.apcata.2017.06.029>.

- [14] C.A. Teles, P.M. de Souza, R.C. Rabelo-Neto, M.B. Griffin, C. Mukarakate, K.A. Orton, D.E. Resasco, F.B. Noronha, Catalytic upgrading of biomass pyrolysis vapors and model compounds using niobia supported Pd catalyst, *Applied Catalysis B: Environmental*. 238 (2018) 38–50. <https://doi.org/10.1016/j.apcatb.2018.06.073>.
- [15] C.A. Teles, P.M. de Souza, R.C. Rabelo-Neto, A. Teran, G. Jacobs, C. Vilela Weikert, Z.M. Magriotis, V.O.O. Gonçalves, D.E. Resasco, F.B. Noronha, Reaction pathways for the HDO of guaiacol over supported Pd catalysts: Effect of support type in the deoxygenation of hydroxyl and methoxy groups, *Molecular Catalysis*. 523 (2022) 111491. <https://doi.org/10.1016/j.mcat.2021.111491>.
- [16] L. Nie, B. Peng, X. Zhu, Vapor-Phase Hydrodeoxygenation of Guaiacol to Aromatics over Pt/HBeta: Identification of the Role of Acid Sites and Metal Sites on the Reaction Pathway, *ChemCatChem*. 10 (2018) 1064–1074. <https://doi.org/10.1002/cctc.201701413>.
- [17] M. Hellinger, H.W.P. Carvalho, S. Baier, D. Wang, W. Kleist, J.-D. Grunwaldt, Catalytic hydrodeoxygenation of guaiacol over platinum supported on metal oxides and zeolites, *Applied Catalysis A: General*. 490 (2015) 181–192. <https://doi.org/10.1016/j.apcata.2014.10.043>.
- [18] J. Zhang, J. Sun, Y. Wang, Recent advances in the selective catalytic hydrodeoxygenation of lignin-derived oxygenates to arenes, *Green Chem*. 22 (2020) 1072–1098. <https://doi.org/10.1039/C9GC02762A>.
- [19] L. Nie, P.M. de Souza, F.B. Noronha, W. An, T. Sooknoi, D.E. Resasco, Selective conversion of m-cresol to toluene over bimetallic Ni–Fe catalysts, *Journal of Molecular Catalysis A: Chemical*. 388–389 (2014) 47–55. <https://doi.org/10.1016/j.molcata.2013.09.029>.
- [20] P.M. de Souza, R.C. Rabelo-Neto, L.E.P. Borges, G. Jacobs, B.H. Davis, T. Sooknoi, D.E. Resasco, F.B. Noronha, Role of Keto Intermediates in the Hydrodeoxygenation of Phenol over Pd on Oxophilic Supports, *ACS Catal*. 5 (2015) 1318–1329. <https://doi.org/10.1021/cs501853t>.
- [21] A.M. Barrios, C.A. Teles, P.M. de Souza, R.C. Rabelo-Neto, G. Jacobs, B.H. Davis, L.E.P. Borges, F.B. Noronha, Hydrodeoxygenation of phenol over niobia supported Pd catalyst, *Catalysis Today*. 302 (2018) 115–124. <https://doi.org/10.1016/j.cattod.2017.03.034>.
- [22] C.A. Teles, R.C. Rabelo-Neto, J.R. de Lima, L.V. Mattos, D.E. Resasco, F.B. Noronha, The Effect of Metal Type on Hydrodeoxygenation of Phenol Over Silica Supported Catalysts, *Catal Lett*. 146 (2016) 1848–1857. <https://doi.org/10.1007/s10562-016-1815-5>.
- [23] C.A. Teles, R.C. Rabelo-Neto, G. Jacobs, B.H. Davis, D.E. Resasco, F.B. Noronha, Hydrodeoxygenation of Phenol over Zirconia-Supported Catalysts: The Effect of Metal Type on Reaction Mechanism and Catalyst Deactivation, *ChemCatChem*. 9 (2017) 2850–2863. <https://doi.org/10.1002/cctc.201700047>.
- [24] P.M. de Souza, R.C. Rabelo-Neto, L.E.P. Borges, G. Jacobs, B.H. Davis, D.E. Resasco, F.B. Noronha, Hydrodeoxygenation of Phenol over Pd Catalysts. Effect of Support on Reaction Mechanism and Catalyst Deactivation, *ACS Catal*. 7 (2017) 2058–2073. <https://doi.org/10.1021/acscatal.6b02022>.
- [25] Q. Tan, G. Wang, A. Long, A. Dinse, C. Buda, J. Shabaker, D.E. Resasco, Mechanistic analysis of the role of metal oxophilicity in the hydrodeoxygenation of anisole, *Journal of Catalysis*. 347 (2017) 102–115. <https://doi.org/10.1016/j.jcat.2017.01.008>.

- [26] C.A. Teles, P.M. de Souza, A.H. Braga, R.C. Rabelo-Neto, A. Teran, G. Jacobs, D.E. Resasco, F.B. Noronha, The role of defect sites and oxophilicity of the support on the phenol hydrodeoxygenation reaction, *Applied Catalysis B: Environmental*. 249 (2019) 292–305. <https://doi.org/10.1016/j.apcatb.2019.02.077>.
- [27] R.B. Levy, M. Boudart, Platinum-Like Behavior of Tungsten Carbide in Surface Catalysis, *Science*. 181 (1973) 547–549. <https://doi.org/10.1126/science.181.4099.547>.
- [28] K.J. Smith, Metal carbides, phosphides, and nitrides for biomass conversion, *Current Opinion in Green and Sustainable Chemistry*. 22 (2020) 47–53. <https://doi.org/10.1016/j.cogsc.2019.11.008>.
- [29] M. Zhou, H.A. Doan, L.A. Curtiss, R.S. Assary, Identification of Active Metal Carbide and Nitride Catalytic Facets for Hydrodeoxygenation Reactions, *J. Phys. Chem. C*. 125 (2021) 8630–8637. <https://doi.org/10.1021/acs.jpcc.1c02387>.
- [30] M.M. Sullivan, C.-J. Chen, A. Bhan, Catalytic deoxygenation on transition metal carbide catalysts, *Catal. Sci. Technol.* 6 (2016) 602–616. <https://doi.org/10.1039/C5CY01665G>.
- [31] S. Boulloussa-Eiras, R. Lødeng, H. Bergem, M. Stöcker, L. Hannevold, E.A. Blekkan, Catalytic hydrodeoxygenation (HDO) of phenol over supported molybdenum carbide, nitride, phosphide and oxide catalysts, *Catalysis Today*. 223 (2014) 44–53. <https://doi.org/10.1016/j.cattod.2013.09.044>.
- [32] H. Wang, S. Liu, K.J. Smith, Synthesis and Hydrodeoxygenation Activity of Carbon Supported Molybdenum Carbide and Oxycarbide Catalysts, *Energy Fuels*. 30 (2016) 6039–6049. <https://doi.org/10.1021/acs.energyfuels.6b01032>.
- [33] T. Zhang, X. Guo, Z. Zhao, Glucose-Assisted Preparation of a Nickel–Molybdenum Carbide Bimetallic Catalyst for Chemoselective Hydrogenation of Nitroaromatics and Hydrodeoxygenation of *m*-Cresol, *ACS Appl. Nano Mater.* 1 (2018) 3579–3589. <https://doi.org/10.1021/acsanm.8b00735>.
- [34] C.-J. Chen, A. Bhan, Mo₂C Modification by CO₂, H₂O, and O₂: Effects of Oxygen Content and Oxygen Source on Rates and Selectivity of *m*-Cresol Hydrodeoxygenation, *ACS Catal.* 7 (2017) 1113–1122. <https://doi.org/10.1021/acscatal.6b02762>.
- [35] W.-S. Lee, A. Kumar, Z. Wang, A. Bhan, Chemical Titration and Transient Kinetic Studies of Site Requirements in Mo₂C-Catalyzed Vapor Phase Anisole Hydrodeoxygenation, *ACS Catal.* 5 (2015) 4104–4114. <https://doi.org/10.1021/acscatal.5b00713>.
- [36] W.-S. Lee, Z. Wang, R.J. Wu, A. Bhan, Selective vapor-phase hydrodeoxygenation of anisole to benzene on molybdenum carbide catalysts, *Journal of Catalysis*. 319 (2014) 44–53. <https://doi.org/10.1016/j.jcat.2014.07.025>.
- [37] Q. Lu, C.-J. Chen, W. Luc, J.G. Chen, A. Bhan, F. Jiao, Ordered Mesoporous Metal Carbides with Enhanced Anisole Hydrodeoxygenation Selectivity, *ACS Catal.* 6 (2016) 3506–3514. <https://doi.org/10.1021/acscatal.6b00303>.
- [38] A.L. Jongerius, R.W. Gosselink, J. Dijkstra, J.H. Bitter, P.C.A. Bruijninx, B.M. Weckhuysen, Carbon Nanofiber Supported Transition-Metal Carbide Catalysts for the Hydrodeoxygenation of Guaiacol, *ChemCatChem*. 5 (2013) 2964–2972. <https://doi.org/10.1002/cctc.201300280>.
- [39] C.-C. Tran, O. Mohan, A. Banerjee, S.H. Mushrif, S. Kaliaguine, A Combined Experimental and DFT Investigation of Selective Hydrodeoxygenation of Guaiacol over Bimetallic Carbides, *Energy Fuels*. 34 (2020) 16265–16273. <https://doi.org/10.1021/acs.energyfuels.0c03102>.

- [40] E. Ochoa, D. Torres, J.L. Pinilla, I. Suelves, Nanostructured Carbon Material Effect on the Synthesis of Carbon-Supported Molybdenum Carbide Catalysts for Guaiacol Hydrodeoxygenation, *Energies*. 13 (2020) 1189. <https://doi.org/10.3390/en13051189>.
- [41] E. Ochoa, D. Torres, J.L. Pinilla, I. Suelves, On the hydrothermal-enhanced synthesis of highly selective Mo₂C catalysts to fully deoxygenated products in the guaiacol HDO reaction, *Journal of Environmental Chemical Engineering*. 9 (2021) 105146. <https://doi.org/10.1016/j.jece.2021.105146>.
- [42] E. Blanco, C. Sepulveda, K. Cruces, J.L. García-Fierro, I.T. Ghampson, N. Escalona, Conversion of guaiacol over metal carbides supported on activated carbon catalysts, *Catalysis Today*. 356 (2020) 376–383. <https://doi.org/10.1016/j.cattod.2019.08.029>.
- [43] S. Liu, H. Wang, K.J. Smith, C.S. Kim, Hydrodeoxygenation of 2-Methoxyphenol over Ru, Pd, and Mo₂C Catalysts Supported on Carbon, *Energy Fuels*. 31 (2017) 6378–6388. <https://doi.org/10.1021/acs.energyfuels.7b00452>.
- [44] J. Pang, J. Sun, M. Zheng, H. Li, Y. Wang, T. Zhang, Transition metal carbide catalysts for biomass conversion: A review, *Applied Catalysis B: Environmental*. 254 (2019) 510–522. <https://doi.org/10.1016/j.apcatb.2019.05.034>.
- [45] J. Lee, Molybdenum carbide catalysts I. Synthesis of unsupported powders, *Journal of Catalysis*. 106 (1987) 125–133. [https://doi.org/10.1016/0021-9517\(87\)90218-1](https://doi.org/10.1016/0021-9517(87)90218-1).
- [46] H. Zou, S. Chen, J. Huang, Z. Zhao, Effect of additives on the properties of nickel molybdenum carbides for the tri-reforming of methane, *International Journal of Hydrogen Energy*. 41 (2016) 16842–16850. <https://doi.org/10.1016/j.ijhydene.2016.07.108>.
- [47] Y. Ma, G. Guan, C. Shi, A. Zhu, X. Hao, Z. Wang, K. Kusakabe, A. Abudula, Low-temperature steam reforming of methanol to produce hydrogen over various metal-doped molybdenum carbide catalysts, *International Journal of Hydrogen Energy*. 39 (2014) 258–266. <https://doi.org/10.1016/j.ijhydene.2013.09.150>.
- [48] Y. Ma, G. Guan, P. Phanthong, X. Hao, W. Huang, A. Tsutsumi, K. Kusakabe, A. Abudula, Catalytic Activity and Stability of Nickel-Modified Molybdenum Carbide Catalysts for Steam Reforming of Methanol, *J. Phys. Chem. C*. 118 (2014) 9485–9496. <https://doi.org/10.1021/jp501021t>.
- [49] A. Zhang, A. Zhu, B. Chen, S. Zhang, C. Au, C. Shi, In-situ synthesis of nickel modified molybdenum carbide catalyst for dry reforming of methane, *Catalysis Communications*. 12 (2011) 803–807. <https://doi.org/10.1016/j.catcom.2011.01.019>.
- [50] K.T. Jung, W.B. Kim, C.H. Rhee, J.S. Lee, Effects of Transition Metal Addition on the Solid-State Transformation of Molybdenum Trioxide to Molybdenum Carbides, *Chem. Mater*. 16 (2004) 307–314. <https://doi.org/10.1021/cm030395w>.
- [51] J.A. Schaidle, N.M. Schweitzer, O.T. Ajenifujah, L.T. Thompson, On the preparation of molybdenum carbide-supported metal catalysts, *Journal of Catalysis*. 289 (2012) 210–217. <https://doi.org/10.1016/j.jcat.2012.02.012>.
- [52] 2019 - SMIRNOV et al. - Hydrogenation of Furfural to 2-Methylfuran over Ni-Mo₂C- γ -Al₂O₃ catalyst.pdf, (n.d.).
- [53] L.A. Sousa, J.L. Zotin, V. Teixeira da Silva, Hydrotreatment of sunflower oil using supported molybdenum carbide, *Applied Catalysis A: General*. 449 (2012) 105–111. <https://doi.org/10.1016/j.apcata.2012.09.030>.

- [54] V. Briois, C. La Fontaine, S. Belin, L. Barthe, T. Moreno, V. Pinty, A. Carcy, R. Girardot, E. Fonda, ROCK: the new Quick-EXAFS beamline at SOLEIL, *J. Phys.: Conf. Ser.* 712 (2016) 012149. <https://doi.org/10.1088/1742-6596/712/1/012149>.
- [55] C. La Fontaine, L. Barthe, A. Rochet, V. Briois, X-ray absorption spectroscopy and heterogeneous catalysis: Performances at the SOLEIL's SAMBA beamline, *Catalysis Today*. 205 (2013) 148–158. <https://doi.org/10.1016/j.cattod.2012.09.032>.
- [56] C. Lesage, E. Devers, C. Legens, G. Fernandes, O. Roudenko, V. Briois, High pressure cell for edge jumping X-ray absorption spectroscopy: Applications to industrial liquid sulfidation of hydrotreatment catalysts, *Catalysis Today*. 336 (2019) 63–73. <https://doi.org/10.1016/j.cattod.2019.01.081>.
- [57] B. Ravel, M. Newville, *ATHENA*, *ARTEMIS*, *HEPHAESTUS*: data analysis for X-ray absorption spectroscopy using *IFEFFIT*, *J Synchrotron Rad.* 12 (2005) 537–541. <https://doi.org/10.1107/S0909049505012719>.
- [58] M. Newville, *IFEFFIT*: interactive XAFS analysis and *FEFF* fitting, *J Synchrotron Rad.* 8 (2001) 322–324. <https://doi.org/10.1107/S0909049500016964>.
- [59] J. Jaumot, A. de Juan, R. Tauler, MCR-ALS GUI 2.0: New features and applications, *Chemometrics and Intelligent Laboratory Systems*. 140 (2015) 1–12. <https://doi.org/10.1016/j.chemolab.2014.10.003>.
- [60] W.H. Cassinelli, L. Martins, A.R. Passos, S.H. Pulcinelli, C.V. Santilli, A. Rochet, V. Briois, Multivariate curve resolution analysis applied to time-resolved synchrotron X-ray Absorption Spectroscopy monitoring of the activation of copper alumina catalyst, *Catalysis Today*. 229 (2014) 114–122. <https://doi.org/10.1016/j.cattod.2013.10.077>.
- [61] J. Hong, E. Marceau, A.Y. Khodakov, L. Gaberová, A. Griboval-Constant, J.-S. Girardon, C.L. Fontaine, V. Briois, Speciation of Ruthenium as a Reduction Promoter of Silica-Supported Co Catalysts: A Time-Resolved in Situ XAS Investigation, *ACS Catal.* 5 (2015) 1273–1282. <https://doi.org/10.1021/cs501799p>.
- [62] L. de Oliveira, K. Bouchmella, A. Picco, L. Capeletti, K. Gonçalves, J.H. dos Santos, J. Kobarg, M. Cardoso, Tailored Silica Nanoparticles Surface to Increase Drug Load and Enhance Bactericidal Response, *J. Braz. Chem. Soc.* (2017). <https://doi.org/10.21577/0103-5053.20170017>.
- [63] M. Thommes, K. Kaneko, A.V. Neimark, J.P. Olivier, F. Rodriguez-Reinoso, J. Rouquerol, K.S.W. Sing, Physisorption of gases, with special reference to the evaluation of surface area and pore size distribution (IUPAC Technical Report), *Pure and Applied Chemistry*. 87 (2015) 1051–1069. <https://doi.org/10.1515/pac-2014-1117>.
- [64] I. Jonane, A. Cintins, A. Kalinko, R. Chernikov, A. Kuzmin, X-ray absorption near edge spectroscopy of thermochromic phase transition in CuMoO_4 , *Low Temperature Physics*. 44 (2018) 434–437. <https://doi.org/10.1063/1.5034155>.
- [65] T. Mo, J. Xu, Y. Yang, Y. Li, Effect of carburization protocols on molybdenum carbide synthesis and study on its performance in CO hydrogenation, *Catalysis Today*. 261 (2016) 101–115. <https://doi.org/10.1016/j.cattod.2015.07.014>.
- [66] H.M. Abdel-Dayem, Dynamic Phenomena during Reduction of $\alpha\text{-NiMoO}_4$ in Different Atmospheres: In-Situ Thermo-Raman Spectroscopy Study, *Ind. Eng. Chem. Res.* 46 (2007) 2466–2472. <https://doi.org/10.1021/ie0613467>.
- [67] Ehrenberg-1995.pdf, (n.d.).
- [68] N. Joseph, J. Varghese, T. Siponkoski, M. Teirikangas, M.T. Sebastian, H. Jantunen, Glass-Free CuMoO_4 Ceramic with Excellent Dielectric and Thermal Properties for Ultralow Temperature Cofired Ceramic Applications, *ACS*

- Sustainable Chem. Eng. 4 (2016) 5632–5639. <https://doi.org/10.1021/acssuschemeng.6b01537>.
- [69] W. Tan, J. Luan, Investigation into the synthesis conditions of CuMoO_4 by an *in situ* method and its photocatalytic properties under visible light irradiation, RSC Adv. 10 (2020) 9745–9759. <https://doi.org/10.1039/D0RA00496K>.
- [70] B. Saravanakumar, G. Ravi, R. Yuvakkumar, V. Ganesh, R.K. Guduru, Synthesis of polyoxometalates, copper molybdate ($\text{Cu}_3\text{Mo}_2\text{O}_9$) nanopowders, for energy storage applications, Materials Science in Semiconductor Processing. 93 (2019) 164–172. <https://doi.org/10.1016/j.mssp.2019.01.002>.
- [71] T. Ressler, R.E. Jentoft, J. Wienold, M.M. Günter, O. Timpe, In Situ XAS and XRD Studies on the Formation of Mo Suboxides during Reduction of MoO_3 , J. Phys. Chem. B. 104 (2000) 6360–6370. <https://doi.org/10.1021/jp000690t>.
- [72] Y. Zheng, Y. Tang, J.R. Gallagher, J. Gao, J.T. Miller, I.E. Wachs, S.G. Podkolzin, Molybdenum Oxide, Oxycarbide, and Carbide: Controlling the Dynamic Composition, Size, and Catalytic Activity of Zeolite-Supported Nanostructures, J. Phys. Chem. C. 123 (2019) 22281–22292. <https://doi.org/10.1021/acs.jpcc.9b05449>.
- [73] A. Kurlov, X. Huang, E.B. Deeva, P.M. Abdala, A. Fedorov, C.R. Müller, Molybdenum carbide and oxycarbide from carbon-supported MoO_3 nanosheets: phase evolution and DRM catalytic activity assessed by TEM and *in situ* XANES/XRD methods, Nanoscale. 12 (2020) 13086–13094. <https://doi.org/10.1039/D0NR02908D>.
- [74] 2000 - BOUCHY et al. - Metastable fcc α -MoC supported on HZSM5 - Preparation and catalytic performance for the non-oxidative conversion of methane to aromatic compounds.pdf, (n.d.).
- [75] B.D. Patterson, R. Abela, Novel opportunities for time-resolved absorption spectroscopy at the X-ray free electron laser, Phys. Chem. Chem. Phys. 12 (2010) 5647. <https://doi.org/10.1039/c003406a>.
- [76] R.P.W.J. Struis, D. Bachelin, C. Ludwig, A. Wokaun, Studying the Formation of Ni_3C from CO and Metallic Ni at $T = 265^\circ\text{C}$ in Situ Using Ni K-Edge X-ray Absorption Spectroscopy, J. Phys. Chem. C. 113 (2009) 2443–2451. <https://doi.org/10.1021/jp809409c>.
- [77] H. Oyanagi, Z.H. Sun, Y. Jiang, M. Uehara, H. Nakamura, K. Yamashita, Y. Orimoto, L. Zhang, C. Lee, A. Fukano, H. Maeda, Small copper clusters studied by x-ray absorption near-edge structure, Journal of Applied Physics. 111 (2012) 084315. <https://doi.org/10.1063/1.3700346>.
- [78] S. Huseyinova, J. Blanco, F.G. Requejo, J.M. Ramallo-López, M.C. Blanco, D. Buceta, M.A. López-Quintela, Synthesis of Highly Stable Surfactant-free Cu_5 Clusters in Water, J. Phys. Chem. C. 120 (2016) 15902–15908. <https://doi.org/10.1021/acs.jpcc.5b12227>.
- [79] N. Mammen, L. Spanu, E.C. Tyo, B. Yang, A. Halder, S. Seifert, M.J. Pellin, S. Vajda, S. Narasimhan, Using first principles calculations to interpret XANES experiments: extracting the size-dependence of the (p , T) phase diagram of sub-nanometer Cu clusters in an O_2 environment, J. Phys.: Condens. Matter. 31 (2019) 144002. <https://doi.org/10.1088/1361-648X/aafcf9>.
- [80] N. Mammen, L. Spanu, E.C. Tyo, B. Yang, A. Halder, S. Seifert, M.J. Pellin, S. Vajda, S. Narasimhan, Reversing Size- Dependent Trends in the Oxidation of Copper Clusters through Support Effects, Eur. J. Inorg. Chem. 2018 (2018) 16–22. <https://doi.org/10.1002/ejic.201701355>.

- [81] C. Nayak, D. Bhattacharyya, S.N. Jha, N.K. Sahoo, In Situ XAS Study on Growth of PVP-Stabilized Cu Nanoparticles, *ChemistrySelect*. 3 (2018) 7370–7377. <https://doi.org/10.1002/slct.201801358>.
- [82] Y. Liu, N. Marcella, J. Timoshenko, A. Halder, B. Yang, L. Kolipaka, Michael.J. Pellin, S. Seifert, S. Vajda, P. Liu, A.I. Frenkel, Mapping XANES spectra on structural descriptors of copper oxide clusters using supervised machine learning, *J. Chem. Phys.* 151 (2019) 164201. <https://doi.org/10.1063/1.5126597>.
- [83] B. Zandkarimi, G. Sun, A. Halder, S. Seifert, S. Vajda, P. Sautet, A.N. Alexandrova, Interpreting the Operando XANES of Surface-Supported Subnanometer Clusters: When Fluxionality, Oxidation State, and Size Effect Fight, *J. Phys. Chem. C*. 124 (2020) 10057–10066. <https://doi.org/10.1021/acs.jpcc.0c02823>.
- [84] A. Halder, C. Lenardi, J. Timoshenko, A. Mravak, B. Yang, L.K. Kolipaka, C. Piazzoni, S. Seifert, V. Bonačić-Koutecký, A.I. Frenkel, P. Milani, S. Vajda, CO₂ Methanation on Cu-Cluster Decorated Zirconia Supports with Different Morphology: A Combined Experimental In Situ GIXANES/GISAXS, Ex Situ XPS and Theoretical DFT Study, *ACS Catal.* 11 (2021) 6210–6224. <https://doi.org/10.1021/acscatal.0c05029>.
- [85] A.A. Dubale, C.-J. Pan, A.G. Tamirat, H.-M. Chen, W.-N. Su, C.-H. Chen, J. Rick, D.W. Ayele, B.A. Aragaw, J.-F. Lee, Y.-W. Yang, B.-J. Hwang, Heterostructured Cu₂O/CuO decorated with nickel as a highly efficient photocathode for photoelectrochemical water reduction, *J. Mater. Chem. A*. 3 (2015) 12482–12499. <https://doi.org/10.1039/C5TA01961C>.
- [86] A. Hanif, T. Xiao, A.P.E. York, J. Sloan, M.L.H. Green, Study on the Structure and Formation Mechanism of Molybdenum Carbides, *Chem. Mater.* 14 (2002) 1009–1015. <https://doi.org/10.1021/cm011096e>.
- [87] K. Oshikawa, M. Nagai, S. Omi, Characterization of Molybdenum Carbides for Methane Reforming by TPR, XRD, and XPS, *J. Phys. Chem. B*. 105 (2001) 9124–9131. <https://doi.org/10.1021/jp0111867>.
- [88] W. Xu, P.J. Ramírez, D. Stacchiola, J.L. Brito, J.A. Rodriguez, The Carburization of Transition Metal Molybdates (MxMoO₄, M = Cu, Ni or Co) and the Generation of Highly Active Metal/Carbide Catalysts for CO₂ Hydrogenation, *Catal Lett.* 145 (2015) 1365–1373. <https://doi.org/10.1007/s10562-015-1540-5>.
- [89] C.G. Silva, F.B. Passos, V.T. da Silva, Influence of the support on the activity of a supported nickel-promoted molybdenum carbide catalyst for dry reforming of methane, *Journal of Catalysis*. 375 (2019) 507–518. <https://doi.org/10.1016/j.jcat.2019.05.024>.
- [90] C.A. Teles, P.M. de Souza, R.C. Rabelo-Neto, A. Teran, G. Jacobs, D.E. Resasco, F.B. Noronha, Hydrodeoxygenation of Lignin-Derived Compound Mixtures on Pd-Supported on Various Oxides, *ACS Sustainable Chem. Eng.* 9 (2021) 12870–12884. <https://doi.org/10.1021/acssuschemeng.1c03720>.